

The BrightEyes-TTM: an Open-Source Time-Tagging Module for Democratising Single-Photon Microscopy

Alessandro Rossetta^{1,2,3,6}, Eli Slenders^{1,6}, Mattia Donato^{1,6}, Eleonora Perego¹, Sabrina Zappone^{1,3}, Francesco Diotalevi⁴, Luca Lanzanò^{2,5}, Sami Koho¹, Giorgio Tortarolo¹, Marco Crepaldi⁴, and Giuseppe Vicedomini^{1,✉}

¹Molecular Microscopy and Spectroscopy, Istituto Italiano di Tecnologia, Via Enrico Melen 85 Bldg. B, 16152, Genoa, Italy

²Nanoscropy and NIC@IIT, Istituto Italiano di Tecnologia, Via Enrico Melen 85 Bldg. B, 16152, Genoa, Italy

³Dipartimento di Informatiche, Bioingegneria, Robotica e Ingegneria dei Sistemi, University of Genoa, Via All'Opera Pia 13, 16145, Genoa, Italy

⁴Electronic Design Laboratory, Istituto Italiano di Tecnologia, Via Enrico Melen 85 Bldg. B, 16152, Genoa, Italy

⁵Dipartimento di Fisica e Astronomia, Università di Catania, Via S. Sofia 64, 95123, Catania, Italy

⁶These authors contributed equally to this work

Fluorescence laser-scanning microscopy (LSM) is experiencing a revolution thanks to new single-photon (SP) array detectors. These detectors give access to an entirely new set of single-photon information typically lost in conventional fluorescence LSM, thus triggering a new imaging/spectroscopy paradigm – the so-called single-photon LSM (SP-LSM). The revolution's outcomes are not only the blooming of new SP-LSM techniques and tailored SP array detectors, but also the need for data-acquisition (DAQ) systems to democratise such innovations. In particular, there is a growing need for (i) DAQ systems capable of handling the high-throughput and high-resolution multi-dimensional photon information generated by the new detectors, and (ii) harmonising these DAQ protocols in existing fluorescence LSMs. To fill this gap, we developed an open-source, low-cost multi-channel time-tagging module (TTM) based on a field-programmable-gate-array (FPGA) that can temporally tag in parallel multiple single-photon events, with 30 ps precision, and multiple synchronisation events, with 4 ns precision. We connected the TTM to an existing fluorescence LSM equipped with a single-photon avalanche diode (SPAD) bi-dimensional array detector, and we implemented super-resolved fluorescence lifetime image scanning microscopy (FLISM) in live-cell. Furthermore, we introduced fluorescence lifetime fluctuation spectroscopy (FLFS), a class of techniques that allows correlating precise information about molecular mobility with fluorescence lifetime, thus opening a new window to deciphering biomolecular processes in live-cell. We expect that our BrightEyes-TTM will support the microscopy community to spread SP-LSM in many life science labs.

single-photon microscopy | fluorescence lifetime image scanning microscopy | fluorescence lifetime fluctuation spectroscopy | time-tagging module | time-to-digital converter | FPGA

Correspondence: giuseppe.vicedomini@iit.it

Main

A revolution is happening in fluorescence laser scanning microscopy (LSM): the radically new way in which the fluorescence signal is recorded with single-photon array detectors drastically expands the information content of any LSM experiment.

For a conventional fluorescence laser scanning microscope, an objective lens focuses the laser beam at a specific position

in the sample, the so-called excitation/probing region. The same objective lens collects the emitted fluorescence and, together with a tube lens, projects the light onto the sensitive area of a single-element detector, such as a photo-multiplier tube (PMT). The probing region is scanned across the sample or kept steady depending on the type of experiment. For imaging, the sample is raster scanned. For single-point fluorescence correlation spectroscopy (FCS), the laser beam is kept steady while for scanning FCS (sFCS) the laser beam is scanned repeatedly in a circular or linear manner on the sample. During the whole measurement, the detector generates a one-dimensional signal (intensity versus time), that the data-acquisition (DAQ) system integrates within the pixel-dwell time (for imaging) or within the temporal bins (for FCS). Such a signal recording process induces information loss: the signal from the fluorescence photons is integrated regardless of their position on the sensitive area and their arrival time with respect to a particular event, such as the fluorophore excitation event. Notably, also other properties of light, such as the wavelength and the polarisation, are typically completely or partially discarded.

New single-photon (SP) array detectors, when combined with adequate DAQ systems, have the possibility to preserve most of this information. In particular, asynchronous read-out SP array detectors (a matrix of fully independent elements able to detect single photons with several tens of picoseconds timing precision) have made it possible to spatiotemporally tag each fluorescence photon, i.e., to record simultaneously at which position of the array (spatial tag) and at which delay with respect to a reference time (temporal tag) the photon hits the detector.

At present, the spatial tags can be used in two ways: firstly, they allow imaging of the probing region by placing a bi-dimensional detector array in the LSM image plane. Secondly, by dispersing the fluorescence across the long axis of a linear detector array, the spatial tags enable spectrally-resolved recording of the probing region, i.e., the spatial tag encodes the wavelength of the photon. At the same time, by exciting the sample with a pulsed laser and recording the fluorescence photon arrival times with respect to the excita-

tion events, these temporal tags (i.e., the time difference between the excitation event and the photon detection) allow for sub-nanosecond time-resolved measurements, such as fluorescence lifetime or photon correlation. Furthermore, recording the photon arrival times with respect to the beginning of the experiment allows for microsecond intensity fluctuation analysis (i.e, microsecond time-resolved spectroscopy).

In summary, these spatial, temporal, and spectral photon signatures have opened a series of advanced fluorescence imaging and spectroscopy techniques precluded to (or made more complex by) conventional single-element detectors. Recently, a new LSM architecture based on SP linear detectors has led to a revival of the combination of fluorescence lifetime and spectral imaging (1) – spectral fluorescence lifetime imaging microscopy (S-FLIM). Simultaneously, bi-dimensional SP array detectors have opened up new perspectives for image-scanning microscopy (ISM). In a nutshell, ISM uses the information contained in the spatial distribution (image) of the probing region to reconstruct the specimen image with a twofold increase in spatial resolution and a higher signal-to-noise ratio (SNR) than conventional LSM (2–4). Because SP bi-dimensional array detectors provide a sub-nanosecond time-resolved image of the probing region, ISM can be combined with fluorescence lifetime to create a super-resolution fluorescence lifetime imaging technique, called fluorescence lifetime ISM (FLISM) (5), or to trigger the implementation of a new class of nanoscopy techniques, namely quantum ISM (Q-ISM) (6). The microsecond time-resolved images can also be used to implement (i) high information content FCS and, more generally, fluorescence fluctuation spectroscopy (FFS) (7) – usually referred to as comprehensive-correlation analysis (CCA) (8); and (ii) the combination of super-resolution optical fluctuation imaging (SOFI) with ISM (9) (SOFISM). Hereafter, we refer to these new techniques with the collective term single-photon laser-scanning microscopy (SP-LSM).

Key elements for implementing SP-LSM are the SP array detector and the DAQ system. Although analogue-to-digital converters (e.g., constant-fraction discriminators) allow the use of photo-multiplier tube arrays as SP detectors, they introduce a significant amount of unwanted correlation into the measurements (10) and are outperformed by true SP detectors regarding the photon-time jitter/precision. An alternative to PMT-based SP array detectors is the AiryScan-inspired module in which the hexagonal-shaped multi-cores fiber bundle is connected to a series of single-element single-photon avalanche diodes (SPADs) (6) instead of PMTs as in the conventional AiryScan module (11). Clearly, this module is expensive and not scalable. True single-photon array detectors based on the well-established SPAD array technology (12, 13) solved these limitations. In particular, new asynchronous read-out SPAD array detectors have been tailored for SP-LSM applications (14–17). These detectors have a small number of elements – but enough for sub-Nyquist sampling of the probing region – high photon-detection efficiency, low dark-noise, high dynamics, high fill-factor, low cross-talk, and low photon time-jitters.

Whilst the development of SPAD array detectors specifically designed for SP-LSM is gaining substantial momentum, no effort has been placed in developing an open-source data acquisition system able to (i) fully exploit the high-throughput and high-resolution photon-level information that these detectors provide; (ii) offer flexibility and upgradability. The lack of an open-source DAQ system may preclude a massive spreading of the above SP-LSM techniques and the emerging of new ones.

To address this need, we propose an open-source multi-channel time-tagging module (TTM), the BrightEyes-TTM, specifically designed to implement current and future fluorescence SP-LSM techniques. In short, the BrightEyes-TTM implements multiple photon- and reference-channels to record at which element of the detector array, and when (with tunable precision), with respect to the reference/synchronisation events, a single-photon reaches the detector. The BrightEyes-TTM is based on a commercially available and low cost field-programmable-gate-array (FPGA) evaluation board, equipped with a state-of-the-art FPGA and a series of I/Os connectors providing an easy interface of the board with the microscope, the SPAD array detector and the computer. We chose an FPGA-based implementation of the module to grant quick prototyping, easy updating and adaptation: in particular, we envisage a module that can be updated – also remotely – by us or other groups to meet the future requests from new SP-LSM techniques and SPAD array detectors.

We integrated the BrightEyes-TTM into an existing SP-LSM equipped with a 25-element SPAD array detector and we used it to perform FLISM imaging on a series of calibration and biological samples, including living cells. Furthermore, for the first time, we demonstrated the combination of CCA with fluorescence lifetime analysis. This synergy opens to a new series of fluorescence lifetime fluctuation spectroscopy (FLFS) techniques able to provide more complete pictures of the biomolecular processes inside living cells. As a proof of principle, we correlated the diffusion mode of a eGFP protein with its fluorescence lifetime.

Despite the great potential of SP-LSM, we are aware that a massive dissemination of this paradigm will be effective only if a broad range of laboratories will have access to the TTM, and potentially modify it according to their needs. For this reason, this manuscript provides detailed guidelines, hardware parts lists, and open-source code for the FPGA firmware and operational software.

Results

Multi-Channel Time-Tagging Module. The BrightEyes-TTM includes multiple fine (picosecond precision) time-to-digital converters (TDCs) to measure the start-stop times and coarse TDCs (nanoseconds precision) to measure the relative delays between photon and clock signals. To characterise the performances of the BrightEyes-TTM, we first used a test bench architecture based on the SYLAP pulse generator to validate the fine TDCs. Independently, we validated the coarse TDCs directly by integrating the TTM into a SP-LSM

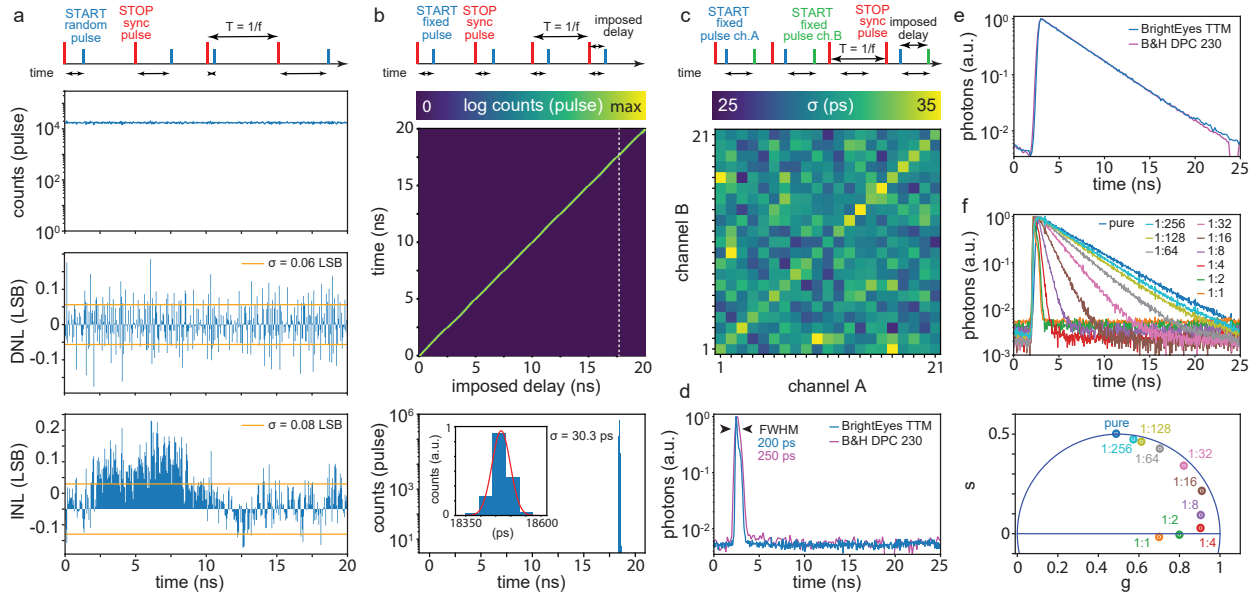


Fig. 1. BrightEyes-TTM characterisation and validation. **a** Statistical code-density test. Temporal schematic representation for the signals involved in the experiment: a fixed frequency SYNC (STOP) clock signal at $f = 50$ MHz (i.e., $\mathcal{T} = 1/f = 20$ ns) and an uncorrelated/random train of pulses (START). The reconstructed start-stop time histogram, i.e., counts versus time (top), the relative differential non-linearity (DNL) (middle) and the integral non-linearity (INL) (lower). **b** Single-shot precision experiment. Temporal schematic representation: a fixed frequency SYNC clock signal and a synchronised but delayed (in a controlled way) signal. Unified representation of the start-stop time histograms as a function of the imposed delay between the two signals (top). Single start-stop time histogram for the delay denoted by the dotted white line in the middle pane (bottom). The inset shows a magnification of the histogram for a selected temporal interval, superimposed with the Gaussian fit (red line). **c** Dual-channel single-shot precision experiment. Temporal schematic representation: a fixed frequency SYNC clock signal and a pair of synchronised signals (channel A and channel B). The delays between all three signals are fixed. Jitter map for each pair of channels (here, 21 channels), i.e., error in the time-difference estimation between any two channels, measured as the standard deviation of a Gaussian fit of the error distribution. The diagonal of the map represents the sigma of the single-channel single-shot precision experiment. **d** Normalised impulse response functions (IRFs) represent the response of the whole architecture (microscope and DAQ) to a fast (sub-nanosecond) fluorescent emission (i.e., start-stop time histogram or TCSPC histogram) for a fluorescein-water solution measured with the BrightEyes-TTM and the DPC-230 card. **e** Normalised fluorescence decay histogram (i.e., start-stop time histogram or TCSPC histogram) for a fluorescein-water solution measured with the BrightEyes-TTM and the DPC-230 card. **f** Normalised fluorescence lifetime decay histograms of quenched fluorescein solutions for increasing concentrations of quencher (potassium iodide) (top), phasor representation of quenched fluorescein solutions (bottom). All single-channel measurements were done with TTM channel #10, which received the photon signal from the central element of the SPAD array detector. All start-stop (i.e., TCSPC) histograms have 48 ps granularity (bin-with).

system.

We measured the linearity of the fine TDCs by performing a statistical code-density test: we fed a fixed-frequency (50 MHz) signal into the synchronisation (SYNC) channel and a random signal in one of the photon channels (here, TTM channel #10). After accumulating several millions of photon events, we built the start-stop time histogram, also called the time-correlated-single-photon counting (TCSPC) histogram, which shows a differential non-linearity (DNL) of $\sigma_{\text{DNL}} = 0.06$ least-significant-bit (LSB) and an integral non-linearity (INL) of $\sigma_{\text{INL}} = 0.08$ LSB (Fig. 1 a) with $\text{LSB} = 48$ ps.

We then measured the single-shot precision (SSP) of the fine TDC by measuring repeatedly a constant start-stop time interval: we fed a fixed-frequency (50 MHz) signal into the SYNC channel and a synchronised second signal – with a tunable fixed delay – into one of the photon channels (here, TTM channel #10). After accumulating several millions of sync-photon pairs, we built the start-stop time histogram, which in this case represents the distribution of the measurement error (Fig. 1 b). By fitting the start-stop time histogram with a Gaussian function, we estimated a precision (standard deviation of the fitted Gaussian distribution) of $\sigma = 30$ ps. We tuned the delay between the two signals across the whole temporal range of the fine TDC (here, 20 ns) and we observed a similar precision for all the imposed delays (Suppl. Fig.

S1), confirming the linearity behaviour of the fine TDC. We repeated the same SPP experiment for the other channels and we obtained a similar precision (diagonal values on matrix of Fig. 1 c).

Furthermore, to confirm the ability of 21 channels (current public BrightEyes-TTM implements up to 21 photon channels) to record photons in parallel, we repeated the SSP experiment by feeding the same signal also into a second photon channel. In this case, the delays between all three signals (Channel_A, Channel_B, and SYNC) were kept fixed, and we used the TTM to measure the delay between the two photon channel signals. Similar to the start-stop time histogram, we built a histogram that reports the elapsed time between the two photon channel signals and we fit the distribution with a Gaussian function. We performed the experiment for all the possible channel pairs and we obtained a σ precision value ranging from 25 to 35 ps, depending on the channel pair (Fig. 1 c).

Next, we integrated the BrightEyes-TTM into a custom-built single-photon laser scanning microscope equipped with a bi-dimensional 25-element SPAD array detector (the 4 corner element are neglected) and a picosecond pulsed diode laser. We used a quenched solution of fluorescein in water, saturated with potassium iodide to measure the impulse-response function (IRF) of the system (18). The relatively

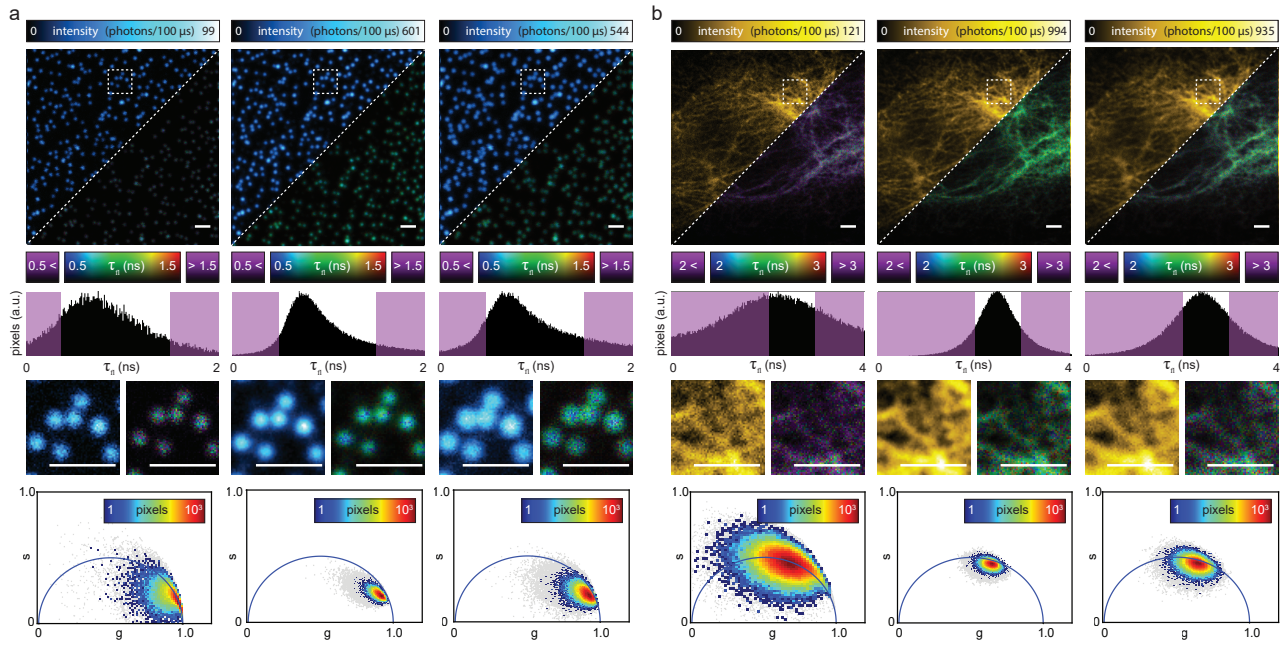


Fig. 2. BrightEyes-TTM for FLISM. **a** Imaging and analysis of 100 nm nanobeads. Side-by-side comparison (top row) of closed confocal (left, pinhole 0.2 AU), adaptive pixel-reassignment ISM (center), and open confocal (right, pinhole 1.4 AU). Each imaging modality shows both the intensity-based image (top-left corner) and the lifetime image (bottom-right corner). A bi-dimensional look-up-table is able to represent in the lifetime images both the intensity values (i.e., photon counts) and the excited-state lifetime values (i.e., τ_{fl}). The intensity-based images integrate the relative 3D data ($x, y, \Delta t$) along the start-stop time dimension Δt . Histogram distributions of the imaging lifetimes values (middle-top row), number of pixels versus lifetime values, - in violet lifetime values which fall out of the selected lifetime interval. The lifetime images report in violet the pixels whose lifetime belongs to this interval. Zoomed regions in the white-dash boxes, the intensity panels are re-normalised to the maximum and minimum values (middle-bottom). Pixel intensity phasor plots (5% and 10% thresholds respectively in grey and color). **b** Imaging and analysis of fluorescently labelled vimentin in fixed cells. Images and graphs appear in the same order as described for (a). Scale bars 2 μ m.

large full-width-at-half-maximum value of the IRF (240 ps) is due to the convolution of the single-shot response (~ 30 ps) with the laser pulse-width (> 100 ps), the SPAD photon jitters (~ 120 ps), and the jitters/dispersion introduced by the optical system (Fig. 1 d). We compared the IRF of the BrightEyes-TTM with the IRF of the DPC-230 commercial multi-channel time-tagging card. Notably, because of the poor time resolution (164 ps from data-sheet), the DPC-230 is not able to reveal the typical cross-talk effect of the SPAD array detector (16), which is visible in the BrightEyes-TTM as an additional bump (Fig. 1 d). We used the two time-tagging systems to compare the decay distributions of a pure (not quenched) solution of fluorescein in water. The two TCSPC histograms show very similar shapes, which is confirmed by fitting them with a single exponential decay model ($\tau_{fl} = 3.97 \pm 0.04$ ns and $\tau_{fl} = 3.99 \pm 0.01$ ns, for the BrightEyes-TTM and the DPC-230, respectively) (Fig. 1 e). To demonstrate the ability of the BrightEyes-TTM to work at different temporal ranges, we repeated the pure fluorescein experiment for different laser frequencies (80, 40, 20, 10 and 5 MHz). The TCSPC histograms do not show significant differences (Suppl. Fig. S2).

To test the BrightEyes-TTM for different fluorescence lifetime values, we measured the decay distributions of the quenched fluorescein solution for increasing concentrations of potassium iodide (Fig. 1 f). The higher the potassium iodide concentration is, the higher the quenching will be, and thus the longer the measurement needs to be in order to accumulate good photon statistics. For this reason, the dark-

noise (which appears as an uncorrelated background in the TCSPC histogram) increases with the quencher concentration. The same effect appears on the phasor-plot: because the decays follow a single-exponential function, caused by the collisional mechanism of the quenching, all points, regardless of the concentration, should lie on the universal semicircle. However, the uncorrelated background shifts the points towards the origin since a lower signal-to-background ratio yields a higher demodulation.

Fluorescence Lifetime Image Scanning Microscopy. To demonstrate the ability of the BrightEyes-TTM in the context of SP-LSM imaging, we implemented FLISM on the same laser-scanning microscope used for the IRF and fluorescein measurements. As with all LSM imaging techniques, FLISM requires acquiring the fluorescence photons in synchronisation with the scanning system (e.g., galvanometer mirrors, acoustic-optics deflectors, and/or piezo stages). We can obtain this synchronisation by measuring the photon arrival times with respect to the clock signals typically provided by the scanning system (i.e., pixel/line/frame clocks). Since the scanning synchronisation does not need a high precision, we can use the reference (REF) channels of the TTM, which use a coarse TDC with nanosecond precision (~ 4.2 ns). Notably, implementing a REF channel using a digital counter-based approach, thus a coarse TDC, consumes fewer FPGA-resources than a high precision channel, which is required for a fine TDC. The current public BrightEyes-TTM has three REF channels, but new version could host more channels with minimal changes in the architecture. For ex-

ample, more REF channels allows recording the photons in synchronisation with a change in the excitation conditions, such as the intensity, the wavelength, or the polarisation.

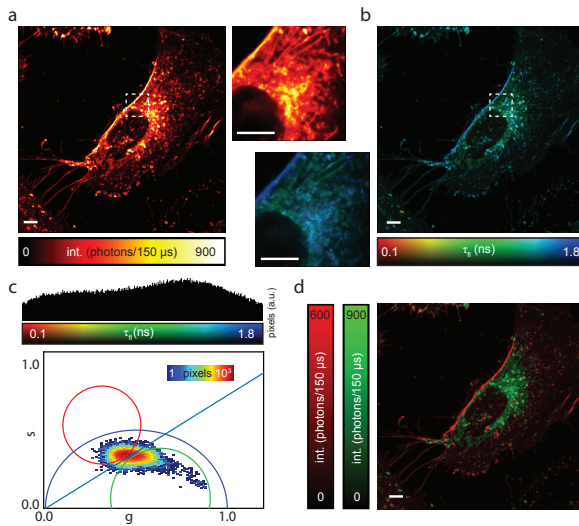


Fig. 3. Fluorescence lifetime image scanning microscopy in live-cells. **a,b**, Intensity-based ISM image (left) and lifetime-based FLISM image (b) of live HeLa cells stained with the polarity-sensitive fluorescent probe di-4-ANEPPDHQ. Side images depict the areas within the dashed white boxes. **c**, Histogram distribution of the imaging lifetimes values (top): number of pixels versus lifetime values. Pixel intensity thresholded phasor plots (bottom): number of pixel versus the polar coordinate (10% thresholds). **d**, Phasor-based segmentation, i.e., images obtained by back-projection of the points within the red (long lifetime, ordered membrane) and green (short lifetime, disordered membrane) circles in the phasor-plot (c). Scale bars 5 μ m.

We connected the pixel, line, and frame clocks delivered by the microscope controlling system to our TTM and we performed 2D imaging of phantom and biological samples. Thanks to the synchronisation signals (SYNC, pixel/line clocks), the stream of photons recorded by the TTM leads to a 4D photon-counting (intensity) image (ch , x , y , Δt), where ch is the dimension describing the channel/element of the SPAD array, (x , y) are the spatial coordinates of the beam scanning system (in these experiments we recorded a single frame), and Δt is the dimension of the TCSPC histogram (Table 3). First, we used the adaptive pixel-reassignment (APR) algorithm (19) to reconstruct the 3D (x , y , Δt) high spatial resolution and high signal-to-noise ratio ISM intensity image. Next, we applied both conventional fluorescence lifetime fitting and phasor analysis to obtain the FLISM (or lifetime) image (x , y) and the phasor plot/histogram (g , s), respectively. The side-by-side comparison of the intensity-based images clearly shows the optical resolution enhancement of ISM with respect to conventional (1.4 AU) imaging and the higher SNR with respect to confocal (0.2 AU) imaging (Fig. 2, top row). The Fourier ring correlation (FRC) analysis confirms the effective resolution enhancement of ISM (Suppl. Fig. S3). In the context of fluorescence lifetime imaging, the higher SNR leads to an higher lifetime precision, as depicted by the lifetime histograms and the phasor plots (Fig. 2, bottom row).

Finally, we used the BrightEyes-TTM for a realistic application of fluorescence lifetime imaging, such as the discrimination of complex microenvironmental variation in a

living cell. In particular, we showed how the fluorescent polarity-sensitive membrane dye di-4-ANEPPDHQ allows monitoring the ordered/disordered-phase membrane domains (15, 20); an important biophysical property which regulates many cellular membrane processes. While the fluorescent dyes in the plasma membrane show relatively long fluorescence lifetimes, denoting a high membrane order, dye molecules in the intracellular membrane show a shorter fluorescence lifetime, denoting a high membrane disorder (Fig. 3 b). We have further highlighted the difference between the two microenvironmental conditions by implementing a phasor-based segmentation 3 c,d).

Because the data collected by the BrightEyes-TTM needs post-processing before being visualised, to obtain a real-time intensity-based image as a guideline during FLISM experiments, we directly implemented in the BrightEyes-TTM a digital output signal which duplicates the signal of one photon channels (e.g., the channel of the central element of the SPAD array). We then sent this duplicate signal to the control system of the microscope (Suppl. Fig. S4), which performs real-time imaging. Notably, this function represents an example of the versatility of the BrightEyes-TTM in the context of imaging.

Fluorescence Lifetime Fluctuation Spectroscopy. To show how the BrightEyes-TTM allows for the study of biomolecular dynamics, we implemented two types of spot-variation FLFS (21): circular scanning FLFS and steady-beam (i.e., single-point) FLFS. In both measurement types, the diffusion dynamics and the fluorescence lifetime can be simultaneously obtained from the absolute times (i.e., the delay of the photons with respect to the beginning of the experiment) t_{photon} and the start-stop times Δt , respectively. Additionally, accessing the start-stop times allows filtering the autocorrelation curves to mitigate artefacts such as detector afterpulsing. As an example for the circular scanning FLFS, we measured freely diffusing fluorescent nanobeads (Fig. 4 (a-c)). From the absolute times, we calculated the unfiltered autocorrelations for the central SPAD array detector element, the sum of the 9 most central elements (called sum 3×3) and the sum over all elements except for the four corner elements (called sum 5×5 here). By scanning the probing region in circle across the sample, the beam waist ω_0 and the diffusion time τ_D can be derived from the same experiment, i.e., no calibration measurement is needed. The fitted diffusion coefficient, $(14.3 \pm 0.5) \mu\text{m}^2/\text{s}$, corresponds to the value that can be expected based on the diameter of the beads. Analysing the diffusion law $\tau_D(\omega_0^2)$ (also called spot-variation analysis) confirms that the beads were freely diffusing: the dependency of τ_D is linear with a zero intercept. However, the fitted concentration of the beads does not scale proportionally to the focal volume, indicating that the amplitude of the autocorrelation functions are not correct. Using the start-stop time histograms, we calculated the filter functions which attenuate the detector afterpulsing and background signals. Applying the filters to the autocorrelation functions significantly alters the amplitudes while the diffusion times are mostly left unchanged. As a result, the fil-

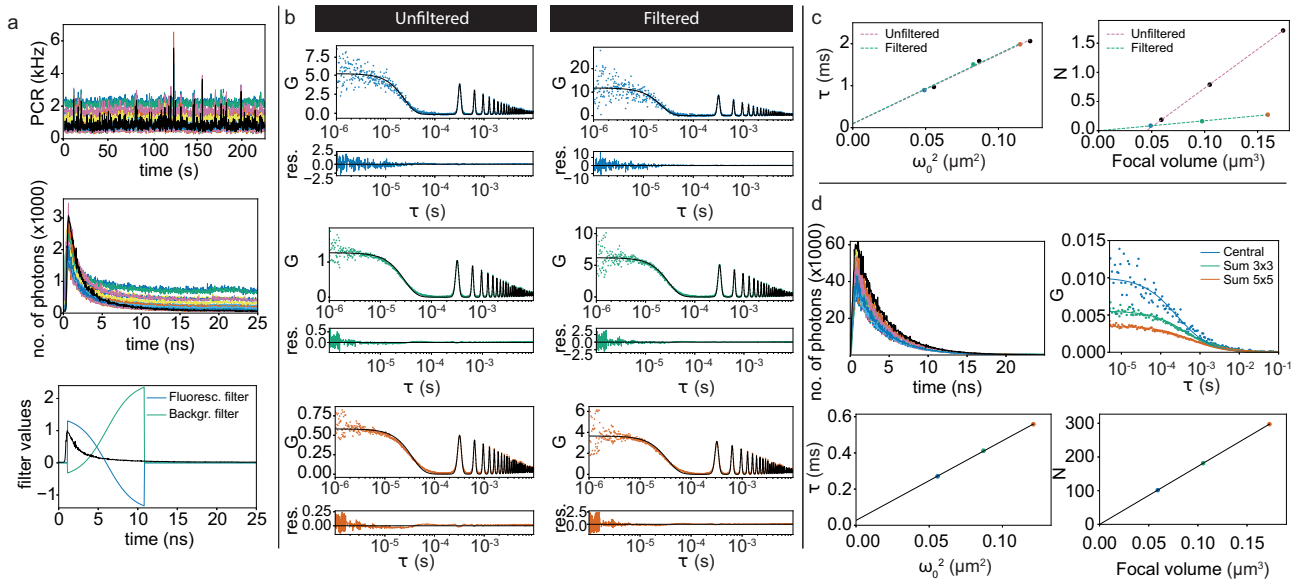


Fig. 4. BrightEyes-TTM for FLFS on freely diffusing fluorescent beads (a-c) and goat anti-mouse antibodies conjugated with Alexa 488 (d). **a** Photon count rate for all channels (top), start-stop time histograms (middle), and filter functions (bottom) for a typical FLCS experiments. The central pixel data is shown in black. **b** Autocorrelations and fits for the central pixel (top), sum 3×3 (middle), and sum 5×5 (bottom), for the unfiltered (left) and filtered (right) case. **c** Diffusion time as a function of ω_0^2 (left) and average number of particles in the focal volume as a function of the focal volume (right). The corresponding diffusion coefficients are $(14.3 \pm 0.5) \mu\text{m}^2/\text{s}$ (unfiltered) and $(14.0 \pm 0.4) \mu\text{m}^2/\text{s}$ (filtered). The fitted particle concentrations are $(7 \pm 3) / \mu\text{m}^3$ (unfiltered) and $(1.70 \pm 0.03) / \mu\text{m}^3$. **d** Start-stop time histograms (top, left), (unfiltered) autocorrelations (top, right), diffusion time as a function of ω_0^2 (bottom, left), and average number of particles in the focal volume (bottom, right). The fitted corresponding diffusion coefficient is $(53 \pm 2) \mu\text{m}^2/\text{s}$ and the particle concentration is $(1720 \pm 4) / \mu\text{m}^3$ (averages and standard deviations over 3 measurements of 130 s each). All start-stop (i.e., TCSPC) histograms have 48 ps resolution (bin-with).

tered autocorrelations show both the expected behaviour for the diffusion time and the concentration (Fig. 4 (a-c)). If the fluorescence signal is strong enough with respect to the background, filtering is not needed, as shown in (Fig. 4 (d)) for freely diffusing goat anti-mouse antibodies conjugated with Alexa 488. Here, the sample and the experimental conditions (e.g., dye concentration and laser power) lead to start-stop time histograms without a significant uncorrelated background. As a result, the correlation curves do not need filtering, and both the diffusion time and the average number of particles in the focal volume follow the expected behaviour.

Especially in a biological context, having simultaneous access to the lifetime (or more in general to the photon-arrival times) and to the diffusion information is not only useful to obtain a robust spot-variation FCS analysis, but also to correlate the mobility mode of the investigated molecules with its microenvironment or its structural changes. Indeed, by using probes sensitive to specific environment states or fluorescence resonance energy transfer (FRET) constructs, the variation of the fluorescence lifetime can be linked to changes in the microenvironment or in the molecular structure. As a proof-of-principle example, we used the BrightEyes-TTM to measure the diffusion of eGFP inside living cells, and correlated its mobility with its fluorescence lifetime (Fig. 5). Notably, because our spot-variation FCS implementation allows extracting the mobility mode from a specific cell position, e.g. the measurement position for single-point FCS, and within a specific temporal window (tens of seconds), it

allows revealing both spatial and temporal heterogeneity in the molecular diffusive behaviour. Spot-variation FCS performed in different cell positions showed free-diffusion dynamics, but different diffusion coefficients (Fig. 5 d), denoting a mobility variability at the single cell level. However, the average diffusion coefficient $D = 34 \pm 12 \mu\text{m}^2/\text{s}$, is well comparable with previous measurements of free eGFP in living cells (17). Repeating the analysis for consecutive time-windows of 5 s each for a single position in the cell shows a temporal variability of the mobility mode (Fig. 5 e). As parameter for the mobility, we calculated the ratio between the diffusion coefficients at different spatial scales, i.e. $D_{\text{central}}/D_{5\times5}$, and we correlated it with the fluorescence lifetime (Fig. 5 f).

Similarly to imaging, we took advantage of the BrightEyes-TTM output signal, which duplicates the central element photon channel, and we fed this signal into the control system of the microscope for a real-time display of the intensity trace and the corresponding autocorrelation function. The autocorrelation obtained from the BrightEyes-TTM is identical to the curve obtained from our National Instruments DAQ reference system (Suppl. Fig. S5): this comparison further validates the proposed TTM.

Discussion

We present a low-cost, open-source, and multi-channel TTM-DAQ system specifically designed for fluorescence SP-LSM: a family of methods which leverage on the possibility of

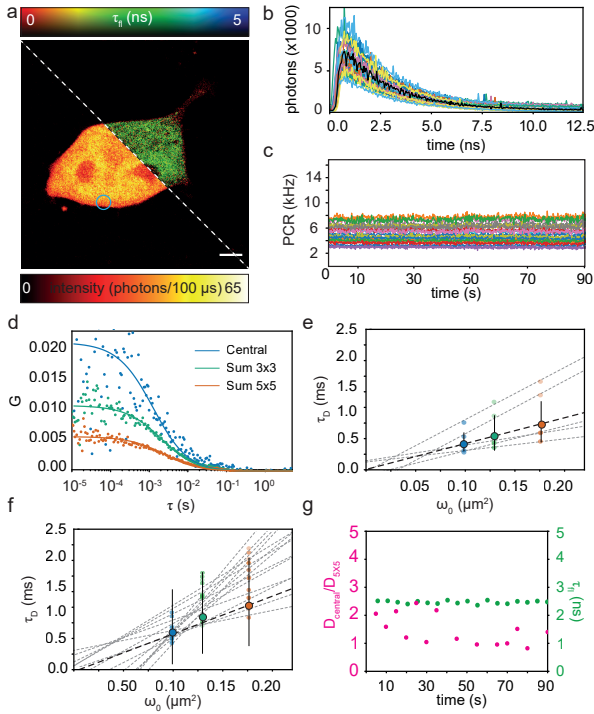


Fig. 5. Fluorescence fluctuation spectroscopy on living cells. **a** ISM (bottom-left corner) and FLISM (top-right corner) images of a HEK293T cell expressing eGFP. **b, c** Start-stop time (or TCSPC) histograms and intensity time-traces for all 25 channels of a 100 s FLCS measurement. The blue spot in (a) depicts the position in the cell where the measurement is performed. **d** Auto-correlation curves (scattered points) and fits (lines) for the central pixel, sum 3×3 , and sum 5×5 curves obtained from (c). **e** Spot-variation analysis (diffusion times as a function of the focal spot size): the dashed black line represents the average ($D = 34 \pm 12 \mu\text{m}^2/\text{s}$, $N = 5$) of the dashed light-grey lines. Each dashed light-grey line represents a different position within the same cell. **f** Spot-variation analysis as a function of the measurement time-coarse. Data from (c). The intensity time-traces (c) are divided in chunks of 5 s, each chunk is analysed by means of spot-variation and generates a dashed light-grey line. The dashed black line represents the average ($D = 32 \pm 5 \mu\text{m}^2/\text{s}$, $N = 14$) of the dashed light-grey lines. **(g)** Ratio between the diffusion coefficients measured for the central pixel and sum 5×5 ($D_{\text{central}}/D_{5 \times 5}$), overlapped with the fluorescence lifetime as a function of the measurement time-coarse. Data from (f). Scale bar 5 μm .

new SP array detectors to analyse the specimen's fluorescence photon-by-photon. We first validated the versatility of the TTM by implementing super-resolution FLISM. Next, to demonstrate the perspectives opened by the TTM, we introduced a brand-new SP-LSM technique, namely FLFS. We recently demonstrated that SPAD array detectors are the method of choice to implement CCA (7). CCA combines – in a single experiment – a series of well-established fluorescence fluctuation spectroscopy approaches to provide a global/comprehensive analysis for deciphering bio-molecular dynamics in living cells. FLFS combines CCA with fluorescence lifetime analysis to further enhance the information content of a single experiment. We used FLFS to monitor the relation between the diffusion mode of an eGFP-tagged protein with its fluorescence lifetime. In this context, we envisage the combination of FLFS with FRET sensors to open new windows to study complex bio-molecular processes under physiological conditions (22).

We implemented the TTM architecture on an FPGA, mounted on a readily available development kit, thus pro-

viding design flexibility and upgradability, and also allowing fast prototyping and testing of new potential BrightEyes-TTM release versions. We anticipate the implementation of a new BrightEyes-TTM version able to handle up to 49 photon channels. Whilst, time-tagging module is the most informative DAQ system, it requires transferring (to the PC) and storing a consistent amount of data. Depending on the applications, this problem can be reduced by performing part of the data analysis and the reconstruction directly on the TTM, by leveraging a novel class of DAQ cards equipped with ARM-based processors.

The principal aim of this work is to democratise single-photon microscopy by giving to any microscopy laboratory the possibility to update their existing LSM systems. The second aim is to trigger the interest of the microscopy community and establish the BrightEyes-TTM as a common platform for further developments in the context of SP-LSM. We are fully aware that these aims can be achieved only if the microscopy maker community (23) has full access to this device, thus we released the results of this work as open-source. In contrast to general purpose commercial TTMs, which typically offer better temporal specifications, our TTM has been designed specifically for fluorescence analysis. Thus, temporal constraints can be relaxed at the benefit of scalability – in terms of photon channels, compatibility with existing LSM systems, and the possibility to integrate new features.

By implementing different low precision reference signals, the TTM can collect photons in synchronisation with many different opto-mechanical devices that could potentially contain, directly or indirectly, additional information about each photon. For example, polarisation modulators and/or analysers can help tagging photons with an excitation and emission polarisation signature. Acoustic tunable filters and spectrometers can provide an excitation and emission wavelength signature.

We anticipate a future for which each single fluorescence photon will be tagged with a series of stamps describing not only its spatial and temporal properties, as shown in this work, but also its polarisation and wavelength characterisations. A series of new algorithms – based on conventional statistical analysis or machine learning techniques, and data-formats will be developed to analyse and store such new multi-parameter single-photon data-sets. Although we believe that the life-science community will receive the major benefits of the SP-LSM technology, allowing them to obtain novel insights about the many bio-molecular processes governing life, we are convinced that SP-LSM will find many applications also in material sciences, in particular in the field of single-dot spectroscopy (24).

Methods

Time-Tagging Module Architecture. In the context of SP-LSM, the goal of the TTM is to tag each photon that reaches the SP detector with a spatial signature and a series of temporal signatures (Suppl. Fig. S6). The spatial signature represents the element of the detector, and thus the spatial position, at which the photon arrives. The temporal signatures are the

delays of the photons with respect to specific events: (i) the fluorophore excitation events induced by a pulsed laser; or (ii) the changes of some experimental condition, e.g., the starting of the experiment (absolute time) or the position change in the probing region. Measuring the photon-arrival time with respect to the excitation event (the so-called start-stop time) typically requires high temporal precision (higher than the SPAD array detectors photon-timing jitters, < 100 ps) and a temporal range larger than the pulse-to-pulse interval of the laser, i.e., 10-1000 ns (for 1-100 MHz laser pulse frequencies). In all other cases, a lower temporal precision (e.g., nanosecond) is needed but the requested temporal range increases up to seconds. To meet these conditions, we implemented different time-to-digital converters (TDCs) for the different types of input signals, i.e., a photon signal, a laser SYNC signal, or a reference (REF) signal. Indeed, the purpose of a TDC is to measure the time interval between two events. In particular, we implemented a fine (picosecond precision) and a coarse (nanosecond precision) TDC.

A fine TDC can be implemented either in an application-specific integrated circuit (ASIC) or on an FPGA. Time-to-digital converters implemented by ASIC can provide a temporal precision much higher than FPGA-based TDCs (sub-picosecond instead of tens of picoseconds) but the latter offer a shorter development cycle and a lower development cost, and they are easily adaptable to new applications. Because (i) our aim was to develop an upgradable TTM, (ii) most fluorescence applications do not require a sub-picosecond temporal precision, and (iii) SPAD array detectors offer a precision of tens of picoseconds, FPGA-based TDCs were the natural choice for our TTM.

Within the FPGA-based TDC, the literature reports several different architectures (25). Each architecture offers a compromise between different specifications (e.g., temporal precision, temporal range, temporal resolution, dead-time, linearity, and FPGA-resources). By using an FPGA, the delay between two events can be easily measured with a counter, which counts the number of clocks between the two events. The counter approach yields a precision no better than the clock period, which is a few nanoseconds for low-cost devices (as in our case) and – in principle – infinite temporal range. While this precision is suitable for measuring the photon-arrival time with respect to second class events, i.e., a change in the experimental conditions (coarse TDC), they do not satisfy the request for the start-stop time assessment. For the delay with respect to the excitation event, a higher precision (10-100 picosecond, depending by the implementation (25)) is achieved by running the photon signal (i.e., the START signal) through a fast tapped-delay-line (TDL), and then measuring the position that is reached when the SYNC signal from the laser (i.e., the STOP signal) is received (fine TDC). The downside of the TDL approach is that the maximum delay measurable (i.e., the temporal range) depends on the length of the TDL, and thus on the available FPGA-resources.

To keep the FPGA-resources low and to implement on the same architecture both a few coarse TDCs for measuring the

second class events as well as one fine TDC for each SPAD array element, we implemented a sliding-scale interpolating TDC architecture (26), also known as the Nutt method (27) (Suppl. Fig. S7). This method uses a pair of tapped delay lines to measure with tens of picoseconds precision the start-stop time, combined with a free-running coarse counter to extend the temporal range. At the same time, the architecture uses the free-running coarse counter to measure the second class events with a few nanoseconds precision. In particular, the architecture combines $N + 1$ ($N = 25$ photon channels in this implementation) tapped delay lines and a coarse counter at 240 MHz to obtain N fine TDCs with tens of picoseconds precision (for the start-stop time of each photon channel), and M coarse TDCs with a nanosecond precision ($M = 3$ reference channels in this implementation). For both TDCs the temporal range is – in principle – limitless. Notably, each fine TDC uses a dedicated START tapped delay line, but shares with the other fine TDCs the STOP delay line: thus, the start-stop time resulting from each fine TDC is measured with respect to the same SYNC signal, which is what is typically needed in all SP-LSM applications. Furthermore, the high frequency clock (240 MHz in our case) allows keeping the delay-lines short (slightly longer than the clock period, i.e., ~ 4.2 ns), thus reducing both the FPGA-resources needed and the dead-time of the fine TDC. Notably, the dead-time of our TDC (~ 4.2 ns) is shorter than (i) typical SPAD detector hold-off times (> 10 ns) and (ii) typical pulsed laser excitation periods for fluorescence applications (12.5–50 ns).

By using two different tapped delay lines for the START and STOP signals, the architecture ensures that the TDCs are asynchronous with respect to the clock counter. The asynchronous design reduces the non-linearity problem of the FPGA-based TDC and auto-calibrates the tapped delay-lines (Supplementary Note 1, Suppl. Fig S8). Here, we describe a single fine TDC, the parallelization to N TDCs is straightforward, and the implementation of the coarse TDC comes naturally with the use of the coarse counter. Each fine TDC is composed by two flash TDCs, each one containing a tapped delay line and a thermometer-to-binary converter (Supplementary Note 3, Suppl. Fig. S9 a-b). The START delay line measures the difference Δt_{START} between the START signal (photon) and the next active edge of the counter clock. Similarly, the STOP delay line measures the difference Δt_{STOP} between the STOP signal (SYNC) and the next active clock rising-edge. Thanks to the free-running coarse counter the architecture is also able to measure n_{photon} and n_{SYNC} , respectively the number of clock cycles between the start of the experiment and the photon (START) signal or the SYNC (STOP) signal. Given these values, (i) the start-stop time Δt is equal to $\Delta t_{\text{STOP}} - \Delta t_{\text{START}} + \Delta n \cdot \mathcal{T}_{\text{sysclk}}$, where $\Delta n = n_{\text{SYNC}} - n_{\text{photon}}$, and $\mathcal{T}_{\text{sysclk}} = 1/240$ MHz is the clock period; (ii) the coarse absolute time \hat{t}_{photon} (i.e., the nanoseconds precision delay of the photon with respect to the beginning of the experiment) is equal to $n_{\text{photon}} \cdot \mathcal{T}_{\text{sysclk}}$. Similarly, the nanosecond delay from the REF signal $\Delta \hat{t}_{\text{REF}}$ is equal to $(n_{(\text{photon})} - n_{\text{REF}}) \cdot \mathcal{T}_{\text{sysclk}}$, where n_{REF} is the number of clock cycles between the beginning of the experiment and

the REF signal. Since the TTM architecture can only provide integer values, a calibration is required to arrive at time values. In particular, the coarse counter provides the values n_{photon} and n_{SYNC} , and the time-to-bin converters of the flash TDCs provide the values ΔT_{photon} and ΔT_{SYNC} . After the raw data is transferred to the PC, the calibration is used to calculate the time values Δt_{photon} and Δt_{SYNC} (Supplementary Note 1), and the application-dependent analysis software allows calculating the time interval between specific events (e.g., Δt , $\Delta \hat{t}_{\text{REF}}^{\text{photon}}$). This approach does not preclude applications in which some other notion of an absolute time is required, such as the absolute photon time (e.g., coarse \hat{t}_{photon} , or fine t_{photon}), rather than the time interval between two events.

The TTM architecture also contains hit-filters (Suppl. Fig. S10), an event-filter (Suppl. Fig. S11), and a data-module in charge of preparing and transferring the data to the PC. The hit-filter is a circuit used to shape and stabilise the input signal. When a hit (photon or SYNC event) occurs, this circuit keeps the signal high until it gets sampled by the internal clock. The hit-filter guarantees the stability of the TDL input signal until the next rising edge event of the internal FPGA clock. The event-filter is a data-input/output filter that reduces the data throughput rate by avoiding to transmit information when no photons are detected. The data-module buffers the data into a FIFO before being transferred to the PC. In its current implementation, data-transfer is done with a USB 3.0 protocol, but it is compatible with other data communication protocols, such as a PCIe.

We implemented the BrightEyes-TTM architecture on a commercially available Kintex-7 FPGA evaluation board (KC705 Evaluation Board, Xilinx), featuring a state-of-the-art FPGA (Kintex-7 XC7K325T-2FFG900C), and – very important for the versatility of the architecture, a series of hardware components (e.g., serial connectors, expansion connectors, and memories). In particular, the different serial connectors potentially allow for different data-transfer rates, and the expansion connectors allow compatibility with other detectors and microscope components (Supl. Fig. S12). Notably, the full TTM system currently implemented uses 75% of the FPGA resources (Suppl. Fig. S13), thus allowing for the introduction of new photon or reference channels or other functions.

To transmit the data to the PC via USB 3.0, current TTM design uses a FX3-based board (Cypress SuperSpeed Explorer kit board, CYUSB3KIT) connected through an adapter card (CYUSB3ACC) to the LPC-FMC connector of the Kintex-7 evaluation board (Supl. Fig. S12). In order to use the FX3, we developed a dedicated module in the FPGA. This module has a simple interface (essentially FIFO with a data-valid flag) for the data transmission and it manages the FX3 control signals and the data-bus. We designed the module to work with the FX3 programmed with the SF_streamIN firmware, which is part of the AN65974 example provided by Cypress. The total component cost for the BrightEyes-TTM is about \$3000.

Test-Bench Architecture and Analysis. We performed the code-density test (Supplementary Note 2) and the single-photon precision measurement by connecting the BrightEyes-TTM to a dedicated signal generator, named SYLAP (Suppl. Fig. S14). We developed SYLAP for this specific project. However, it can help any application which requires synchronised signals with a tunable delay. We implemented SYLAP on an FPGA-evaluation board identical to the one used for the BrightEyes-TTM (i.e., KC705 Evaluation Board, Xilinx). The SYLAP architecture generates a fixed frequency clock, which we used to simulate the laser SYNC signal, and a synchronised pulse train, which we used to simulate the photon signal. Key features of the SYLAP are (i) the possibility to adjust the delay from the clock and the pulse with a granularity of 39.0625 ps; (ii) the possibility to set the clock period and the pulse duration with a granularity of 2.5 ns. The native USB 2.0 serial port of the evaluation board allows configuring the SYLAP. The timing jitter between the clock and the pulse is 13 ps, measured with Keysight DSO9404A 4 GHz bandwidth oscilloscope. Since both the BrightEyes-TTM and the SYLAP signal generator use the same type of board, we also implemented both systems on the very same FPGA (thus the same board). Importantly, in this internal implementation of SYLAP we separated the clock-domains and the clock sources of the two projects. We performed a single-photon precision experiment to compare the stand-alone SYLAP configuration (i.e., two different boards connected with coaxial cables), with the internal configuration, and we did not observe substantial differences. The SYLAP internal implementation demonstrates the flexibility of our TTM architecture in integrating new features.

To perform the code-density test (Supplementary Note 2) we used the clock signal from SYLAP (as SYNC signal) and the TTL signal from an avalanche photo diode (APD, SPCM-AQRH-13-FC, Perkin Elmer) as random photon signals (i.e., temporally correlated). We illuminated the APD with natural light, maintaining a photon-flux well below the saturation value of the detector.

To perform the single-photon precision experiment for all photon channels of the TTM, we took again advantage of the flexibility of our TTM architecture, and in particular the possibility to reprogram the FPGA according to different requests. Indeed, we implemented physical switches which allow simultaneously connecting a single input channel of the board to all photon channels. This feature gives the possibility to measure the same event with all photon channels.

Single-Photon Microscope. Optical Architecture. To test the BrightEyes-TTM, we used a custom-built SP laser-scanning microscope (Suppl. Fig. S15) previously implemented to demonstrate confocal-based FFS with SPAD array detectors (7). In short, the microscope uses a 485 nm pulsed laser (LDH-D-C-485 PicoQuant, driven by a PicoQuant PDL 828 Sepia II Multichannel Picosecond Diode Laser driver) for excitation with a tunable repetition rate f (in this work we used 5, 10, 20, 40, 80 MHz). After passing through a 488/10 nm clean-up filter, the laser light was reflected by a dichroic

beam splitter (ZT405/488/561/640 rpc, Chroma Technology Corporation) towards the galvanometric scanning mirrors. The scanning system was coupled to a 50 mm Leica scan lens and a 200 mm Leica tube lens. We performed all measurements with a $100\times/1.4$ Leica objective lens. Focusing, axial scan, and scouting of the sample region-of-interest were performed with a 3-axis stage (Nano-LP Series, Mad City Labs). The fluorescence signal was collected in de-scanned mode, in which it passed through the dichroic beam splitter, a 488 nm long pass filter and a fluorescence emission filter (ET550/25, Chroma Technology Corporation). A 250 mm lens conjugated with the scan lens was installed to obtain a 1.4 Airy unit field of view on the SPAD array detector, which meant that the detector also acted as a pinhole to remove the out-of-focus fluorescence background. The measurements were performed with a 5×5 SPAD array detector fabricated using BCD technology (16). The hold-off time was set to 100 ns.

Control System. To control the SP laser-scanning microscope, we built a LabVIEW system inspired by the Carma control system (15, 28). The LabVIEW software uses an FPGA-based National Instrument (NI) data-acquisition-card (NI USB-7856R; National Instruments) to control all microscope instruments, such as the galvano-metric mirrors, the 3-axis piezo stage, and the SPAD array detector (through an initialisation protocol). The pixel, line, and frame clocks were delivered as digital outputs. Finally, the control system was able to record the photon signal from the SPAD array detector and transfer the data to the PC (via USB 2.0), where the LabVIEW software allowed real-time visualisation of the images in the case of imaging or the intensity time-traces in the case of FFS. Notably, when the SP laser-scanning microscope was used in time-tagging modality, the photons-signals were delivered to the BrightEyes-TTM. In this case, the BrightEyes-TTM read the photon-signal thanks to a custom I/Os daughter card connected via the FPGA mezzanine connector (FMC) (Supl. Fig. S12). The same card was used to deliver the duplicate signal of the central element of the SPAD array to the LabVIEW control system. The pixel, line, and frame signal passed through a custom-made buffer to match the impedance between the NI and the Xilinx FPGA card. The SYNC signal provided by the laser driver was converted from NIM to TTL (NIM2TTL Converter, MPD) and read by the Xilinx DAQ cards via a SMA digital input. The data recorded by the BrightEyes-TTM were transferred to a PC via USB 3.0. To compare the TTM with a commercial reference system, the SYNC (NIM) signal and the signal from the central element of the SPAD array could also be sent to a commercial TTM card (DPC-230, Becker & Hickl GmbH), running on a dedicated PC.

Data Transfer. The data structure. To transfer the data from the TTM to the PC, we designed a simple data protocol, whose major advantage is the scalability to add photon channels, as well as its flexibility. In a nutshell, the protocol perceives the SP detector array as a fast camera with a maximum frame-rate of 240 MHz, i.e., the frequency at which the whole TTM architecture works. Under this scenario, the data protocol foresees a unique frame-like data structure streamed

to the communication port (in this implementation the USB 3.0) in 32-bits long words (Suppl. Fig. S16). Since the current Bright-Eyes TTM version can read 21 photon channels, it needs to transmit one header word and seven payload words (3 photon channels *per* payload word), thus 256 bits in total. To check the data receiving order and to avoid misinterpretation, each word includes 4 bits as identifier (ID). The first word (header, ID = 0) includes the following information: (i) three bits used as boolean-flag for the reference (REF) events (in our applications the pixel, line, and frame clocks); (ii) the 8 bits representing the value measured by the tap-delay line of the SYNC channel ΔT_{STOP} (in our application the synchronisation signal from the pulsed laser), and (iii) the SYNC data valid boolean-flag which confirms that a SYNC event has occurred; (iv) the 16 bits representing the number of clock cycles of the free-running 240 MHz counter. The successive payload words (ID > 0) contain the information of three photon channels. For each photon channel the word contains: (i) the 8 bits representing the value measured by the tap-delay line of the respective photon channel $\Delta T_{START}(ch)$; (ii) the channel data-valid boolean-flag which confirms that an event in that channel has occurred. Each payload word contains also a general purpose single bit, which can be used to implement another REF_N signal.

Since the data structure is 256 bit long and, in principle, we have to transmit the structure with a rate of 240 MHz, the data throughput would be 7.68 Gbps. However, the USB 3.0 has an effective bandwidth of 3 Gbps. For this reason, the data structure is transmitted only if one of the following conditions occurs: (i) a START event in one of the photon channels, e.g., a photon event; (ii) a STOP event following a START event, e.g., a laser SYNC event occurs after a photon event (event filter); (iii) a REF event, e.g., a pixel/line/frame event; (iv) a force-write event. The force-write event is fundamental for reconstructing any time measurement (relative or absolute) that requires the coarse counter values. Indeed, since the data structure uses only 16 bit for storing the 240 MHz course counter value, the counter needs to reset every 273 μ s. To guarantee the possibility to always reconstruct the relative or absolute value for each event, we implemented an internal trigger which forces to transmit the data structure at least once every 17 μ s, value that corresponds to one sixteenth of the coarse counter reset period.

To improve the robustness of the data transfer process, we mitigated the data throughput peaks by buffering the data in a large (512 kB) BRAM-FIFO on the same FPGA. The TTM code contains a mechanism that guarantees that in case the FIFO gets filled over a certain threshold, i.e., the average data throughput exceeds the USB 3.0 data bandwidth (because of PC latency, a high rate of events, or other reasons), the TTM enters temporarily in a fail-safe mode, giving priority to some type of events. For example, in the case of imaging, the TTM gives priority to the pixel/line/frame flags and to the force-write events. This strategy guarantees the reconstruction of the absolute time of each event (photon or REF) and the image.

In current TTM-implementation, a USB 3.0 effectively trans-

fers the data to the PC. Here, the data receiver software checks the data integrity of the data structures received (i.e. the IDs must be in the correct order) and, if the data structure is properly received, it sequentially writes the data to the raw file without any processing (raw data). The data receiver uses the *libusb-1.0* and is developed in the C programming language (Suppl. Fig. S17).

The pre-processing. To create a user-friendly data-set (Suppl. Fig. S18), we pre-processed the raw data-set. Since the free-running counter has 16 bits, it resets every $273\ \mu s$; therefore, to obtain a consistent monotonic counter n , we update the 16 bits long free-counter provided by the data structure: when the free-counter value is lower than the one in the previous data structure, the value 2^{16} is added to it and added to the following counter values.

With the monotonic counter n , it is possible to calculate the arrival time of each photon event with respect to a REF event or with respect to the SYNC event (start-stop time). While the former calculation is trivial, the latter is more complex. Since the TTM architecture uses a start-stop reverse strategy to reconstruct the photon start-stop time – for a given channel ch , it is necessary to recover the information about successive SYNC laser events. Notably, this information can be contained in the same data structure of the photon, or in a successive data-structure. The pre-processing step identifies for each STOP (SYNC) event the corresponding START (photon) event and creates a table. Each table row contains a STOP (SYNC) event and includes: (i) the relative monotonic counter n_{SYNC} ; (ii) the relative TDL value ΔT_{STOP} ; an entry for each photon event linked to this specific STOP (SYNC) event. In particular, each entry contains: (i) the number of elapsed clock cycles $\Delta n(ch) = n_{\text{SYNC}} - n_{\text{photon}}(ch)$; (ii) the TDL value $\Delta T_{\text{START}}(ch)$.

To simplify the reconstruction of the image, in this phase we also pre-processed the REF information for the pixel/line/frame. We used the pixel/line/frame events to include in the table the columns x , y and fr . Namely, the pixel event increases the x counter; in case of the line event, the x counter resets and the line counter y increases; in case of the frame event, both the x , y counters reset, and the fr counter increases.

We saved the pre-processed dataset in a single compressed HDF5 file composed by different tables: the main table and the 21 tables referred to as the photon channels. All tables use a unique column identifier (idx) which allows the applications software (e.g., FLISM software, FLCS software) to easily merge the information. The main table has a row for each SYNC channel event. Each row contains the corrected monotonic counter n_{SYNC} , the coordinates x , y , fr , the TDL value ΔT_{STOP} value, and the unique row index idx . The photon channel tables have a row for each photon. Each row contains the TDL value $\Delta T_{\text{START}(ch)}$, the elapsed clock cycle $\Delta n(ch)$, and the index idx of the row of the corresponding sync event.

The calibration. Notably, the HDF5 file contains all the information as received by the TTM, but structured in a way that is much easier to access. However, this information still

contains numbers of cycles or tapped-delays. A calibration offline phase allows transforming this information in temporal information. In particular, the calibration (Supplementary Note 1, Suppl. Fig S19) transforms each TDL value $\Delta T_{\text{START}}(ch)$ or ΔT_{SYNC} in a temporal value $\Delta t_{\text{START}}(ch)$ or Δt_{SYNC} , which we can use to calculate all (both relative and absolute) temporal signatures of each event. The output of the calibration is again an HDF5 file, with a structure similar to the uncalibrated file. The main table has a row for each SYNC channel event. Each row contains the absolute SYNC time $t_{\text{SYNC}} = n_{\text{SYNC}} \cdot \tau_{\text{sysclk}} + \Delta t_{\text{SYNC}}$, the coordinates x , y , fr and a unique row index idx . The photon channel tables have for each row the start-stop time $\Delta t(ch)$, and the index idx of the row of the corresponding SYNC event.

The application-dependent analysis. Depending on the application, we further processed the calibrated HDF5. In general, any application requires the generation of the start-stop time (or TCSPC) histogram, which is simply the histogram of a series of Δt values. Because of the auto-calibration steps (Supplementary Note 1), the Δt values are float values, thus the bin-with of the histogram (i.e., the temporal resolution) can be chosen almost arbitrarily by the user. In this work, we used 48 ps, which is a value well below the system IRF (200 ps, Fig. 1) and in the range of the average delay values of the elements (i.e., CARRY4) used to build the tapped delay lines (Supplementary Note 1). In the case of FLISM analysis, the calibrated data are binned into a multidimensional intensity (photon-counting) array ($ch, x, y, fr, \Delta t$). The Δt dimension is the start-stop histogram for the given other coordinates. This multidimensional array can be saved in HDF5 and processed with *ad hoc* scripts or software like ImageJ. The other dimensions ch , x , y , fr are self-explainable. In the case of FFLS analysis, we ignored the x , y and fr information of the calibrated HDF5 and we did not apply any further processing. Indeed, the FFLS needs a list of photon events for each channel, in which each photon has an absolute time – with respect to the beginning of the experiment, and the start-stop time (Δt). By using t_{SYNC} as absolute time (instead of t_{photon} the calibrated HDF5 file contains already all information structured in the best way.

FLISM and FFLS Analysis. *FLISM Reconstruction and Analysis.* We reconstructed the ISM images by using the adaptive pixel-reassignment method (15). In short, we integrated the 4D dataset ($ch, x, y, \Delta t$) along the Δt dimension, we applied a phase-correlation registration algorithm to align all the images ($x, y | ch$) with respect to central image. The registration generated the so called shift-vector fingerprint ($s_x(ch), s_y(ch)$). To obtain the ISM intensity-based images, we integrated the shifted dataset along the ch dimension. To obtain the lifetime-based ISM image, we started from the 4D dataset ($ch, x, y, \Delta t$); for each Δt value we used the same shift-vector fingerprint to shift the relative 2D image; we integrated the result along the ch dimension (Supl. Fig. S20); we used the resulting 3D dataset ($x, y, \Delta t$) and the FLIMJ software (29) to obtain the τ_{fl} maps/images (fitted with a single-exponential decay model). Alternatively, we applied the phasor analysis on the same 3D dataset. We calculated

the phasor coordinates (g, s) using cosine and sine summations (30, 31) (Supl. Fig. S21). To avoid artefacts, we did the MOD mathematical operation of the TCSPC histograms with the laser repetition period value (31). To calibrate the acquisition system and thus to account for the instrument response function of the complete setup (microscope, detector and TTM), measurements were referenced to a fluorescein solution.

To demonstrate the spatial resolution enhancement achieved by ISM, we performed a Fourier ring correlation (FRC) analysis (32, 33). The FRC analysis requires two "identical" images obtained from two different measurements in order to contain different noise realisations. The two images are correlated to obtain the effective cut-of-frequency (i.e., the frequency of the specimen above the noise level) of the images, and thus the effective resolution. Since in this work we built up the images photon-by-photon, we can use the temporal tags of the photons to generate simultaneously two 4D data-sets ($ch, x, y, \Delta t$). Successively, we used the two data-sets to reconstruct the two statistically independent ISM images for the FRC analysis. In particular, we odd-even sort each photon in the two images by using the ΔT_{START} and ΔT_{STOP} integer values. As explained for the sliding-scale approach, the photons are distributed uniformly across the START and STOP tapped-delay lines, thus the method generates two statistical independent data-sets with similar photons counts.

Correlation Calculation and Analysis. We calculated the correlations directly on the lists of the photon absolute times (34). For the sum 3×3 and sum 5×5 analysis, the lists of all the relevant SPAD channels were merged and sorted. Then, the data was split into chunks of 10 or 5 s, for the beads and for eGFP in living cells, respectively, and for each chunk the correlation was calculated. The individual correlation curves were visually inspected and all curves without artefacts were averaged. To obtain the filtered correlation curves, the same procedure was followed, except that a weight was assigned to each photon based on its start-stop time (35, 36). The weights were obtained from the start-stop time histograms of each channel. Only photons in time bins between the peak of the histogram and about 10 ns later were included. In this way, photons that are likely to not originate from the sample were removed. First, the TCSPC histogram of each channel was fitted with a single exponential decay function $H(t) = A \exp(-t/\tau_{fl}) + B$, with the amplitude A , lifetime τ_{fl} , and offset B as free fit parameters. The filters were calculated assuming a single exponential decay with amplitude 1 and lifetime τ_{fl} for the fluorescence histogram and a uniform distribution with value B/A for the after-pulse component. Then, for each photon, a weight was assigned equal to the value of the fluorescence filter function at the corresponding photon start-stop time. E.g., photons that were detected directly after the laser pulse were assigned a higher weight than photons detected some time later, since the probability of a photon being a fluorescence photon decreases with increasing start-stop time. The second filter function was not used for further analysis, since it would amplify the after-pulse component and attenuate the fluorescence contribution.

Both for single-point and circular-scanning (37) FCS, the correlation curves were fitted with a 1-component model assuming a Gaussian detection volume (i.e., probing region, or point spread function, PSF) as described in (17). For the circular FCS measurements (37), the periodicity and radius of the scan movement were kept fixed while the amplitude, diffusion time, and PSF size were fitted. For the conventional FCS measurements, the PSF size was kept fixed at the values found with the circular scanning FCS, and the amplitude and diffusion time were fitted. Since we approximated the PSF as a 3D Gaussian function with a $1/e^2$ lateral radius of ω_0 and a $1/e^2$ height of $k \times \omega_0$ (with k the eccentricity of the detection volume, $k = 4.5$ for central element analysis, $k = 4.1$ for sum 3×3 and sum 5×5 analysis), the diffusion coefficient D can be calculated from the diffusion time τ_D and the PSF size ω_0 via $D = \omega_0^2/(4\tau_D)$.

Samples Preparations. For TTM characterisation and validation, we used fluorescein (46955, free acid, Sigma-Aldrich, Steinheim, Germany) and potassium iodide (KI) (60399-100G-F, BioUltra, $>= 99.5\%$ (AT), Sigma-Aldrich). We dissolved fluorescein from powder into DMSO and then we further diluted to a 1:1000 v/v concentration by adding ultrapure water. For the fluorescein quenching experiments we diluted the 1:1000 fluorescein solution at different ratio with the KI quencher (from 1:2 to 1:256). All samples were made at room temperature. A fresh sample solution was prepared before each measurement.

For imaging experiments we used: (i) a sample of 100 nm fluorescent beads (yellow-green FluoSpheres Q7 Carboxylate-Modified Microspheres, F8803; Invitrogen). We treated the glass coverslips with poly-L-lysine (0.1% (w/v) in H₂O, P8920, Sigma-Aldrich) for 20 min at room temperature, and we diluted the beads in Milli-Q water by 1:10000 v/v. We drop-casted the beads onto the coverslip, and, after 10 min, we washed the coverslip with Milli-Q water, we dried under nitrogen flow, and we mounted overnight with Invitrogen ProLong Diamond Antifade Mounting Medium (P36965); (ii) a prepared microscope slide (IG-4011 Imaging Set, Abberior) containing fixed mammalian cells in which vimentin filaments were stained with STAR-GREEN dye; (iii) a fresh prepared microscope slide containing fixed HeLa cells stained for α -tubulin. We cultured HeLa cells in Dulbecco's Modified Eagle Medium (DMEM, Gibco, ThermoFisher Scientific, Wilmington) supplemented with 10% fetal bovine serum (Sigma-Aldrich) and 1% penicillin/streptomycin (Sigma-Aldrich) at 37 °C in 5% CO₂. The day before immunostaining, we seeded HeLa cells onto coverslips in a 12-well plate (Corning Inc., Corning, NY). The day after, we incubated cells in a solution of 0.3% Triton X-100 (Sigma-Aldrich) and 0.1% glutaraldehyde (Sigma-Aldrich) in the BRB80 buffer (80 mM Pipes, 1 mM EGTA, 4 mM MgCl₂, pH 6.8, Sigma-Aldrich) for 1 min. We fixed HeLa cells with a solution of 4% paraformaldehyde (Sigma-Aldrich) and 4% sucrose (Sigma-Aldrich) in the BRB80 buffer for 10 min and then we washed three times for 15 min in phosphate-buffered saline (PBS, Gibco™, ThermoFisher). Next, we treated the cells with a solution of

0.25% Triton-X100 in the BRB80 buffer for 10 min and we washed three times for 15 min in PBS. After 1 h in blocking buffer (3% bovine serum albumin (BSA, Sigma-Aldrich) in BRB80 buffer), we incubated the cells with monoclonal mouse anti- α -tubulin antibody (1:1000, Sigma-Aldrich) diluted in the blocking buffer for 1 h at room temperature. The alpha-tubulin goat anti-mouse antibody was revealed by Alexa Fluor 488 goat anti-mouse (1:1000, Invitrogen, ThermoFisher Scientific) incubated for 1 h in BRB80 buffer. We rinsed HeLa cells three times in PBS for 15 min. Finally, we mounted the cover slips onto microscope slides (Avantor, VWR International) with ProLong Diamond Antifade Mountant (Invitrogen, ThermoFisher Scientific). (iv) Live cell imaging of HeLa cells stained for di-4-ANEPPDHQ. The day before live cell imaging, we seeded HeLa cells onto a μ -Slide 8-well plate (Ibidi, Grafelfing, Germany). Just before the measurement, cells were incubated with DMEM (Gibco, Thermo Fisher Scientific) supplemented with 5 μ M of di-4-ANEPPDHQ (Invitrogen, ThermoFisher Scientific) at 37 °C in 5% CO₂ for 30 min. Cells were washed three times with DMEM. Measurements were performed in Live Cell Imaging Solution (Thermo Fisher Scientific) at room temperature. For fluorescence fluctuation spectroscopy experiments we used: (i) YG carboxylate fluoSpheres (REF F8787, 2% solids, 20 nm diameter, actual size 27 nm, exc./em. 505/515 nm, Invitrogen, ThermoFisher) diluted 5000 \times in ultrapure water. A droplet was poured onto a cover slip for the FLFS measurements; (ii) goat anti-Mouse IgG secondary antibody with Alexa Fluor 488 sample (REF A11029, Invitrogen, ThermoFisher). The antibody was diluted 100 \times in PBS to a final concentration of 20 μ g/mL. 200 μ L of the resulting dilution was poured into an 8 well chamber previously treated with a 1% BSA solution to prevent the sample to stick to the glass. All samples were made at room temperature. A fresh sample solution was prepared for each measurement. (iii) HEK293T cells expressing monomeric eGFP. HEK293T cells were cultured in DMEM (Dulbecco's Modified Eagle Medium, Gibco™, ThermoFisher Scientific) supplemented with 1% MEM (Eagle's minimum essential medium), Non-essential Amino Acid Solution (Sigma-Aldrich), 10% fetal bovine serum (Sigma-Aldrich) and 1% penicillin/streptomycin (Sigma-Aldrich) at 37 °C in 5% CO₂. HEK293T cells were seeded onto a μ -Slide 8-well plate (Ibidi GmbH). HEK293T cells were transfected with pcDNA3.1(+)-eGFP (Addgene plasmid #129020). Transfection was performed using Effectene® Transfection Reagent (Qiagen, Hilden, Germany) according to manufacturer's protocol. Measurements were performed in Live Cell Imaging Solution (ThermoFisher Scientific) at room temperature.

Data availability

As keen proponents of open science and open data, we have made the raw time-tagged data, which supports the findings of this study, publicly available at Zenodo, <https://doi.org/10.5281/zenodo.4912656>. Full build instructions for the BrightEyes-TTM is available through our GitHub repository

<https://github.com/VicidominiLab/BrightEyes-TTM>.

Code availability

The firmware and the VHDL/Verilog source code for implementing time-tagging on the FPGA evaluation board, the data-receiver software to install on the personal computer, and the operational software with are accessible through the Vicidomini Lab GitHub <https://github.com/VicidominiLab/BrightEyes-TTM>.

ACKNOWLEDGEMENTS

This research was supported by Fondazione San Paolo, "Observation of biomolecular processes in live-cell with nanocamera", No. EPFD0098 (E.S. and G.V.) and by the European Research Council, Bright Eyes, No. 818699 (G.T. and G.V.) and by the European Union's Horizon 2020 research and innovation programme under the Marie Skłodowska-Curie grant agreement no. 890923 (SMSPAD) (E.S.). We thank Prof. Alberto Diaspro and Dr. Paolo Bianchini (Nanoscopy & NIC@IIT, Istituto Italiano di Tecnologia) for useful discussions; Dr. Michele Oneto (Nikon Imaging Center) and Marco Scotto (Molecular Microscopy and Spectroscopy, Istituto Italiano di Tecnologia) for support on the experiments; Alessandro Barcellona (Electronic Design Laboratory, Istituto Italiano di Tecnologia) for design and implementation of the custom-made buffer ; Prof. Alberto Tosi, Prof. Federica Villa, Dr. Mauro Buttafava (Politecnico di Milano), Dr. Marco Castello, and Dr. Simon-Luca Piazza (Istituto Italiano di Tecnologia and Genoa Instruments) for useful initial discussions in the time-to-digital design and for the realisation of the single-photon avalanche-diode detector array.

AUTHOR CONTRIBUTIONS

G.V. conceived the idea and designed the research; G.V. and M.C. supervised the research, A.R., M.D., and F.D. wrote the firmware for the time-tagging module and the data-receiver; M.D. with support from A.R. wrote the operational software; A.R., E.S., M.D., S.K., and G.T. wrote the imaging analysis software; E.S., M.D., and L.L. wrote the FFS analysis software; A.R. and M.D., characterised and validate the TTM module with the test-bench architecture; E.S. build the single-photon microscopy; S.Z. prepared the cell samples. E.S. and E.P. with support from A.R. performed the single-photon microscopy experiments; A.R., E.S., M.D., E.P., S.K., G.T., and G.V., analysed the data. A.R., M.D. and G.V., build the GitHub repository; G.V., with supports from A.R., E.L., and M.D., wrote the manuscript with edits from all authors.

COMPETING FINANCIAL INTERESTS

G.V. has personal financial interest (co-founder) in Genoa Instruments, Italy; A.R. has personal financial interest (founder) in FLIM labs, Italy outside the scope of this work.

Bibliography

- Scipioni, L., Rossetta, A., Tedeschi, G. & Gratton, E. Phasor s-FLIM: a new paradigm for fast and robust spectral fluorescence lifetime imaging. *Nat. Methods* (2021).
- Bertero, M., Mol, C. D., Pike, E. & Walker, J. Resolution in diffraction-limited imaging, a singular value analysis. iv. the case of uncertain localization or non uniform illumination object. *Optica Acta: International Journal of Optics* **31**, 923–946 (1984).
- Sheppard, C. J. R. Super-resolution in confocal imaging. *Optik* **80**, 53–54 (1988).
- Müller, C. B. & Enderlein, J. Image scanning microscopy. *Phys. Rev. Lett.* **104**, 198101 (2010).
- Castello, M., Diaspro, A. & Vicidomini, G. Multi-images deconvolution improves signal-to-noise ratio on gated stimulated emission depletion microscopy. *Appl. Phys. Lett.* **105**, 234106 (2014).
- Tenne, R. *et al.* Super-resolution enhancement by quantum image scanning microscopy. *Nat. Photonics* **13**, 116–122 (2018).
- Slenders, E. *et al.* Confocal-based fluorescence fluctuation spectroscopy with a SPAD array detector. *Light Sci. Appl.* **10** (2021).
- Scipioni, L., Lanzanò, L., Diaspro, A. & Gratton, E. Comprehensive correlation analysis for super-resolution dynamic fingerprinting of cellular compartments using the zeiss airyscan detector. *Nature Communications* **9** (2018).
- Sroda, A. *et al.* SOFISM: Super-resolution optical fluctuation image scanning microscopy. *Optica* **7**, 1308 (2020).
- Brown, C. M. *et al.* Raster image correlation spectroscopy (RICS) for measuring fast protein dynamics and concentrations with a commercial laser scanning confocal microscope. *J. Microsc.* **229**, 78–91 (2008).
- Huff, J. The airyscan detector from ZEISS: confocal imaging with improved signal-to-noise ratio and super-resolution. *Nat. Methods* **12**, i–ii (2015).
- Zappa, F., Tisa, S., Tosi, A. & Cova, S. Principles and features of single-photon avalanche diode arrays. *Sensors and Actuators A: Physical* **140**, 103–112 (2007).
- Bruschini, C., Homulle, H., Antolovic, I. M., Burri, S. & Charbon, E. Single-photon avalanche diode imagers in biophotonics: review and outlook. *Light: Science & Applications* **8** (2019).
- Antolovic, I. M., Bruschini, C. & Charbon, E. Dynamic range extension for photon counting arrays. *Opt. Express* **26**, 22234 (2018).
- Castello, M. *et al.* A robust and versatile platform for image scanning microscopy enabling super-resolution FLIM. *Nat. Methods* **16**, 175–178 (2019). (preprint on bioRxiv).

16. Buttafava, M. *et al.* SPAD-based asynchronous-readout array detectors for image-scanning microscopy. *Optica* **7**, 755 (2020).
17. Slenders, E. *et al.* Cooled SPAD array detector for low light-dose fluorescence laser scanning microscopy. *Biophysical Reports* **1**, 100025 (2021).
18. Liu, M. *et al.* Instrument response standard in time-resolved fluorescence spectroscopy at visible wavelength: Quenched fluorescein sodium. *Applied Spectroscopy* **68**, 577–583 (2014).
19. Koho, S. V. *et al.* Two-photon image-scanning microscopy with SPAD array and blind image reconstruction. *Biomed. Opt. Express* **11**, 2905 (2020).
20. Owen, D. M. *et al.* Fluorescence lifetime imaging provides enhanced contrast when imaging the phase-sensitive dye di-4-ANEPPDHQ in model membranes and live cells. *Biophys. J.* **90**, L80–L82 (2006).
21. Wawrzynieck, L., Rigneault, H., Marguet, D. & Lenne, P.-F. Fluorescence correlation spectroscopy diffusion laws to probe the submicron cell membrane organization. *Biophys. J.* **89**, 4029 – 4042 (2005).
22. Hellenkamp, B. *et al.* Precision and accuracy of single-molecule FRET measurements—a multi-laboratory benchmark study. *Nat. Methods* **15**, 669–676 (2018).
23. Owens, B. The microscope makers. *Nature* **551**, 659–662 (2017).
24. Lindquist, N. C., de Albuquerque, C. D. L., Sobral-Filho, R. G., Paci, I. & Brolo, A. G. High-speed imaging of surface-enhanced raman scattering fluctuations from individual nanoparticles. *Nat. Nanotechnology* **14**, 981–987 (2019).
25. Machado, R., Cabral, J. & Alves, F. S. Recent developments and challenges in FPGA-based time-to-digital converters **68**, 4205–4221 (2019).
26. Tontini, A., Gasparini, L., Pancheri, L. & Passerone, R. Design and characterization of a low-cost FPGA-based TDC **65**, 680–690 (2018).
27. Nutt, R. Digital time intervalometer. *Rev. Sci. Instrum.* **39**, 1342–1345 (1968).
28. Castello, M. *et al.* Universal removal of anti-stokes emission background in sted microscopy via fpga-based synchronous detection. *Rev. Sci. Instrum.* **88**, 053701 (2017).
29. Gao, D. *et al.* FLIMJ: An open-source ImageJ toolkit for fluorescence lifetime image data analysis. *PLOS One* **15**, e0238327 (2020).
30. Digman, M. A., Caioffa, V. R., Zamar, M. & Gratton, E. The phasor approach to fluorescence lifetime imaging analysis. *Biophys. J.* **94**, L14–L16 (2008).
31. Ranjit, S., Malacrida, L., Jameson, D. M. & Gratton, E. Fit-free analysis of fluorescence lifetime imaging data using the phasor approach. *Nature Protocols* **13**, 1979–2004 (2018).
32. Tortarolo, G., Castello, M., Diaspro, A., Koho, S. & Vicidomini, G. Evaluating image resolution in sted microscopy. *Optica* **5**, 32–35 (2018).
33. Koho, S. *et al.* Fourier ring correlation simplifies image restoration in fluorescence microscopy. *Nat. Commun.* **10**, 3103 (2019). (preprint on [bioRxiv](#)).
34. Wahl, M., Gregor, I., Patting, M. & Enderlein, J. Fast calculation of fluorescence correlation data with asynchronous time-correlated single-photon counting. *Opt. Express* **11**, 3583 (2003).
35. Enderlein, J. & Gregor, I. Using fluorescence lifetime for discriminating detector afterpulsing in fluorescence-correlation spectroscopy. *Rev. Sci. Instrum.* **76**, 033102 (2005).
36. Kapusta, P., Macháň, R., Benda, A. & Hof, M. Fluorescence lifetime correlation spectroscopy (FLCS): Concepts, applications and outlook. *Int. J. Mol. Sci.* **13**, 12890–12910 (2012).
37. Petrášek, Z., Derenko, S. & Schwille, P. Circular scanning fluorescence correlation spectroscopy on membranes. *Opt. Express* **19**, 25006 (2011).

Supplementary Note 1: Sliding-Scale Technique and Auto-Calibration

The sliding scale approach is the most suitable FPGA-based TDC architecture for the BrightEyes-TTM as it incorporates crucial features for single-photon microscopy applications. In fact, the sliding-scale design allows for a flexible multi-channel TDC implementation, which reduces the well-known non-linearity problem of FPGA-based TDCs and minimises FPGA resources, allowing the BrightEyes-TTM to be used with different laser sync rates, granting moreover, the auto-calibration of the TTM.

The sliding-scale technique uses multiple flash TDC modules, one for each implemented channel (START channels), and a dedicated one for the STOP channel (i.e. the laser SYNC signal), deployed in the FPGA together with a coarse free-running digital counter (Suppl. Fig. S7). A key feature of this technique is the synchronous readout of the flash TDC and the coarse counter, together with the FPGA internal reference clock, which is totally uncorrelated with respect to the STOP signal and therefore also to the photon arrival time. The sliding-scale technique can thus be defined as an asynchronous design (1–3). An advantage of this design is that all the input signals (START_N and $\text{STOP}_{\text{SYNC}}$) produce time-tagging values over the full available dynamic range of the flash TDC. In short, the very same experiment can be used for calibration (e.g., estimate for each delay unit of the flash TDC module the effective duration, Suppl. Note 3) independently of all flash TDCs, and to further compensate for the non-linearity.

Sliding scale technique. To tackle the linearity issue, the fundamental sliding scale TDC architecture is composed of a flash TDC module to sample START events (i.e. incoming photons) and a second flash TDC module to acquire the STOP signal (i.e. the laser sync signal) (Suppl. Fig S8). As described in literature (4), a conventional FPGA-based flash TDC should not be used implemented because of its lack of linearity across the probed temporal range, caused by intrinsic non-linearities in the FPGA fabric. The non-linear behaviour of flash TDC modules is shown in Figure S8 (a). In the sliding scale technique, instead of using a single flash TDC in which the delays between the STARTs and STOP signals are directly measured, two independent flash TDC modules are used in combination with a coarse counter. One flash TDC measures Δt_{photon} , i.e., the arrival time of the photon (START) with respect to an internal FPGA reference clock. The second TDC measures Δt_{SYNC} , i.e., the delay of the laser sync (STOP) with respect to the same FPGA reference clock, Fig S8 (a). The coarse counter is needed to calculate the time difference (Δt) between the photon and the laser pulse, Eq. S1 (see also Fig S8 a):

$$\Delta t = \underbrace{[n_{\text{SYNC}} \cdot \mathcal{T}_{\text{sysclk}} - \Delta t_{\text{SYNC}}]}_{t_{\text{SYNC}}} - \underbrace{[n_{\text{photon}} \cdot \mathcal{T}_{\text{sysclk}} - \Delta t_{\text{photon}}]}_{t_{\text{photon}}} \quad (\text{S1})$$

Since the photon and laser sync signal are asynchronous with respect to the FPGA clock, the same time interval Δt is measured in different regions of the flash TDC module for different photons. In the sliding scale approach, identical time intervals will therefore yield slightly different flash TDC responses. However, these non-linearities are averaged out over multiple observations (Suppl. Fig. S8 b). In order to reduce FPGA consumption (to further allow scaling up the current design) and to take advantage of the TTM auto-calibration system described below, the calculations and time conversions for computing Δt , Δt_{photon} and Δt_{SYNC} take place on a host computing unit during a post-processing phase. Here, the flash-TDC readings and the registered coarse counter values are merged for each channel to reconstruct the history of each photon (Suppl. Fig. S16). In the proposed TTM architecture, the conjunction of separate flash TDC modules and a common 16 bit-wide coarse free-running counter for all the implemented channels not only levels out the non-linearity but also offers the possibility to (i) keep track of the experiment time, allowing the TTM to have a virtually infinite temporal range, and (ii) to deal with different laser sync rates. Together with the photons and laser sync arrival times, the wrapping events of the coarse counter are also registered and used to calculate the experiment time by simply combining the number of wraps with the period of the FPGA reference clock (240 MHz i.e. ~4.2 ns). The ability of the TTM to reconstruct the time axis based on the internal FPGA clock also allows the TTM to be used with different laser sync frequencies without needing to change the FPGA firmware. As a result, the TTM can be used to work at different temporal ranges, having always the same linear response.

Auto-calibration. Thanks to the sliding-scale approach, the TTM calibration procedure can be carried out directly on the same experiment data. In order to calibrate a flash TDC module (i.e. assessing the time width of all the small delay elements that constitute a flash TDC, Suppl. Note 3) a statistical code density test needs to be performed (Suppl. Note 2). By sampling and accumulating random photon events, one can build up a look-up-table (LUT) that contains the time-conversion factors of all the possible TDC readouts to time-tag the incoming photons. In the sliding-scale approach, all the input signals (photons and laser sync events) are, by default, unsynchronized with the FPGA clock. The statistical code density test is thus built-in into the tagging architecture mechanism design: the TTM can be calibrated with experiment data, hence the name auto-calibration. All the deployed flash TDC modules are calibrated bin-by-bin in a post-processing phase using the reconstructed experiment data. In this way, voltage and temperature changes will not affect the data and timing reconstruction. In conclusion, although the auto-calibration is conducted off-line (i.e., not in real-time), it has the advantage that no ad-hoc calibration acquisitions are needed and, since it can be implemented on the computer, it does not need extra resources on the FPGA chip.

Bin-by-bin calibration. In the sliding scale approach, the flash TDC clock (FPGA clock) is not correlated with the START_n or STOP inputs, i.e., all measured inputs have the same probability of falling into any bin of the tapped delay line of the flash TDC module (Suppl. Fig. S9 a). Since the bin widths (i.e. the delay element values of the tapped delay line) are not all equal due to the intrinsic FPGA irregularities, a photon or sync hit is more likely to fall into a wider bin than into a narrower bin (4). In order to calibrate the time response of the TTM, the histograms of the hit counts as a function of the arrival bin of each deployed flash TDC module are used. After having collected a large number of START_n or STOP events from a measurement, the cumulative event count in each bin is proportional to its width. For example, if a total of N hits are accumulated into the histogram (Suppl. Fig. S19 a), assuming these hits are evenly spread over ~4.2 ns, which is the period of 240 MHz FPGA clock driving the flash TDC, then the width of an N_i-count bin is w_i = N_i*(4200 ps)/(N) (Suppl. Fig. S19 b). In the bin-by-bin calibration procedure, the widths w_i of all tapped delay line CARRY elements (Suppl. Note 3) are measured and stored in an array w_k, then the calibrated time responses Δt_i, corresponding to the center of i-th bin, can be calculated according to Eq. S2 below (5, 6):

$$\Delta t_i = \frac{w_i}{2} + \sum_{k=0}^{i-1} w_k \quad (\text{S2})$$

In this way, all the different Δt_i time contributions of all the flash TDC module delay elements, can be assessed and used to correctly time-tag both the photons (START_n) and the laser sync line (STOP) (Suppl. Fig. S19 c).

TCSPC histogram binning. Since we use the sliding-scale (or Nutt) method to implement the fine TDC, and an off-line (post-acquisition) bin-by-bin calibration, the user can arbitrary choose the bin width of the start-stop (TCSPC) histogram. In this work we always used the same bin width value, i.e., 48 ps. We used this value for the code density test (i.e., least-significant-bit (LSB) is equal to 48 ps), for the single-shot precision measurements, and for all the experimental measurements. This value is much lower than the system IRF full-width-at-half maximum (200 ps), and it is in the same range of the CARRY's average temporal length, i.e., the length of the tapped delay elements used to implement the TDC. Supplementary Fig. S22 shows the calculated (bin-by-bin calibrated) w_k bin widths for all the N = 21 deployed flash-TDC modules in a typical code-density experiments. The average values for the bin widths is 43 ± 25 ps. Notably, this information is not used in any TCSPC histogram reconstruction, since the bin width is arbitrary choose by the user. Supplementary Figure S23 shows the very same start-stop histogram (i.e., the same experiment) for different bin-width values. The histogram changes substantially shape only for bin-width higher than the with of the system IRF. This value is lower than the system IRF full-width-at-half maximum (200 ps) and in the same range of the CARRY's temporal length. The average of the calculated (bin-by-bin calibrated) w_k bin widths for all the N = 21 deployed flash-TDC modules is 48 ps. For this reason, 48 ps is chosen as the LSB value and used as the standard bin width to create the photon count histograms. Since we use the Nutt-sliding scale module and off-line post-acquisition calibration, the bin width can be virtually chosen to be any value greater than 48 ps (Suppl. Fig. S23).

Supplementary Note 2: Statistical Code Density Test

The code density test allows measuring (i) the time response of each time-bin of the TDC and (ii) the deviation of TTM measurement readouts from the actual time of arrival of a photon. One of the most important parameters to analyse in order to asses the system response of a time-tagging device is the system linearity. A statistical code density test consist of feeding TTM random (uncorrelated) photons with respect to the sync reference signal. Here, we generated random photons by connecting an avalanche photodiode (APD) to the TTM in a no-light room (Suppl. Fig S14). After reconstructing the histogram H_(i) of the collected random events (using bin-by-bin auto-calibrated data), H_(i) histogram data is used to compute two benchmark indicators of a system's linearity: the differential non-linearity (DNL) and the integral non-linearity (INL) (Suppl. Fig 1 a). The DNL and INL may seem counter-intuitive indices as the DNL describes the non-linearity amongst the different time-bins of H_(i) (i.e., how much all the bin widths in the temporal range differ from each other) and the INL to what extent the system is non-linear (i.e., to what extent the system is capable of precisely measuring time with respect to an ideal time-tagging device). The relevant values are the standard deviations of the DNL and INL, which are expressed in LSB. In agreement with the Xilinx Kintex-7 XC7K325T-2FFG900C datasheet, an LSB of 48 ps, corresponding to the time delay associated with the coarseness of the CARRY4 element (employed as the fundamental unit in the flash TDC module) was used to reconstruct H_(i) and compute σ_{DNL} and σ_{INL} (7).

DNL - Differential non-linearity. When performing a statistical code density test, the reconstructed time histogram H_(i) should ideally be a constant flat line, indicating that every time-bin has an equal time-width within the measured temporal range. In reality, due to intrinsic FPGA fabric inconsistencies, H_(i) shows a ripple that needs to be characterised in order to maximise the timing precision and accuracy. The aim of computing the DNL is to understand to which degree the difference in time widths of all the possible time bins (which is the cause of the ripple) deviates from a common average value. In other words, the DNL is used to understand the relative contribution of all the time bins when reconstructing times of arrival of photons in the TDC temporal range. The DNL is calculated according to Eq. S3:

$$DNL_{(i)} = \frac{H_{(i)} - H_{\text{avg}}}{H_{\text{avg}}} \quad (\text{S3})$$

Here, $H_{(i)}$ is the reconstructed histogram of the dark counts and H_{avg} its average value. $DNL_{(i)}$ represents the deviation of the i -th time bin from the H_{avg} value: the lower this deviation, the flatter the $DNL_{(i)}$ plot will be. If the DNL is constant, all time-bins have the same width and the system is perfectly linear. Having set the LSB to 48 ps, σ_{DNL} is about 6 % of the LSB, yielding an RMS value of 2.88 ps: on average the time width of the histogram bins is thus: 48 ± 3 ps.

INL - Integral non-linearity. The INL is used to determine to which degree the response of a time-tagging system differs from the ideal linear behaviour. The INL gives an estimate of the difference between a TTM measurement and the actual time of arrival of a photon. If the TTM is linear, the INL is constant and zero.

The $INL_{(i)}$ is computed as the cumulative sum of all the $DNL_{(i)}$ contributions, Eq. S4:

$$INL_{(i)} = \sum_{k=1}^i DNL_{(k)} \quad (\text{S4})$$

The σ_{INL} for all the TTM channels is 8 % of the LSB, which corresponds to an RMS value of 3.84 ps.

Supplementary Note 3: Flash TDC module

In this supplementary section, we describe the principal components and the associated functions that constitute the flash TDC module used in the TTM architecture. The core constituent of a flash TDC module is a tapped delay line (TDL). The TDL is constituted by a series of small delay elements joined in a chain architecture and is used to delay an input (START) signal with respect to a reference-sampling FPGA digital clock. From the delay characteristics of each delay element, it is possible to match the distance covered by the START signal along the delay line with a specific arrival time (time-tag) with respect to the FPGA clock signal (8, 9), Fig S8 a.

Tapped Delay Line and latch barrier. A specific Xilinx FPGA primitive function block known as CARRY (CARR4 or CARRY8 depending on the FPGA family) was used as a fundamental delay block to build the tapped delay line, formed by connecting multiple CARRY blocks. Each delay block is connected to a latch component that can retain either a boolean '0' or '1' depending on the data input value at the rising-edge of an FPGA clock. Assuming that the START signal is '0' (false) at the steady state and '1' (true) after a triggering event, the '1' value will propagate through the tapped delay line elements and consequently the data input of each latch (bit_n) will also change from '0' to '1'. The START signal propagates freely until a rising-edge of the FPGA clock occurs. This rising-edge freezes the values of the latch barrier connected to the TDL elements giving out a digital reading of how far the START signal travelled along the TDL within the FPGA internal clock period. Knowing the reciprocal relationship between the CARRY delay value (and also knowing the delay contribution of each CARRY element in the chain) and the distance the START signal covered before the rising-edge of the FPGA clock occurred, it is possible to convert the digital measurement of the travelled distance into a time measurement (10), Suppl. Fig. S9 a.

Thermometer to binary encoder. The readout from the latch barrier is a series of '1' and '0' that have to be converted into a binary value for a more efficient representation. Therefore, a dedicated circuit is needed to interpret and decode the TDL data. The thermometer-like readout coming from the latch barrier is sent to a thermometer to binary encoder component (T2B). The T2B accepts an array of n-bits as input and returns a binary number that represents how many '1' are present in the input latched data. This T2B conversion simplifies the TDL readout, allowing for a more effective data registration in terms of memory resources utilisation (11), Suppl. Fig. S9 b.

Bibliography

1. Bayer, E. & Traxler, M. A high-resolution (< 10 ps RMS) 48-channel time-to-digital converter (TDC) implemented in a field programmable gate array (FPGA). *IEEE Transactions on Nuclear Science* **58**, 1547–1552 (2011).
2. Tontini, A., Gasparini, L., Pancheri, L. & Passerone, R. Design and characterization of a low-cost FPGA-based TDC **65**, 680–690 (2018).
3. Tancock, S., Arabul, E. & Dahouni, N. A review of new time-to-digital conversion techniques. *IEEE Transactions on Instrumentation and Measurement* **68**, 3406–3417 (2019).
4. Wu, J. & Shi, Z. The 10-ps wave union TDC: Improving FPGA TDC resolution beyond its cell delay. In *2008 IEEE Nuclear Science Symposium Conference Record* (IEEE, 2008).
5. Liu, C. & Wang, Y. A 128-channel, 710 m samples/second, and less than 10 ps RMS resolution time-to-digital converter implemented in a kintex-7 FPGA. *IEEE Transactions on Nuclear Science* **62**, 773–783 (2015).
6. Carra, P. *et al.* Auto-calibrating TDC for an SoC-FPGA data acquisition system. *IEEE Transactions on Radiation and Plasma Medical Sciences* **3**, 549–556 (2019).
7. Villa, F. *et al.* CMOS SPADs with up to 500 μm diameter and 55% detection efficiency at 420 nm. *Journal of Modern Optics* **61**, 102–115 (2014).
8. Klär, H., Schulz, M., Steffen, P. & Düllmann, D. The flash-TDC. *Nuclear Instruments and Methods in Physics Research Section A: Accelerators, Spectrometers, Detectors and Associated Equipment* **275**, 197–198 (1989).
9. Parsakordasiabi, M., Vornicu, I., Rodríguez-Vázquez, Á. & Carmona-Galán, R. A low-resources TDC for multi-channel direct ToF readout based on a 28-nm FPGA. *Sensors* **21**, 308 (2021).
10. Favi, C. & Charbon, E. A 17ps time-to-digital converter implemented in 65nm FPGA technology. In *Proceeding of the ACM/SIGDA international symposium on Field programmable gate arrays - FPGA '09* (ACM Press, 2009).
11. Homulle, H., Regazzoni, F. & Charbon, E. 200 MS/s ADC implemented in a FPGA employing TDCs. In *Proceedings of the 2015 ACM/SIGDA International Symposium on Field-Programmable Gate Arrays* (ACM, 2015).

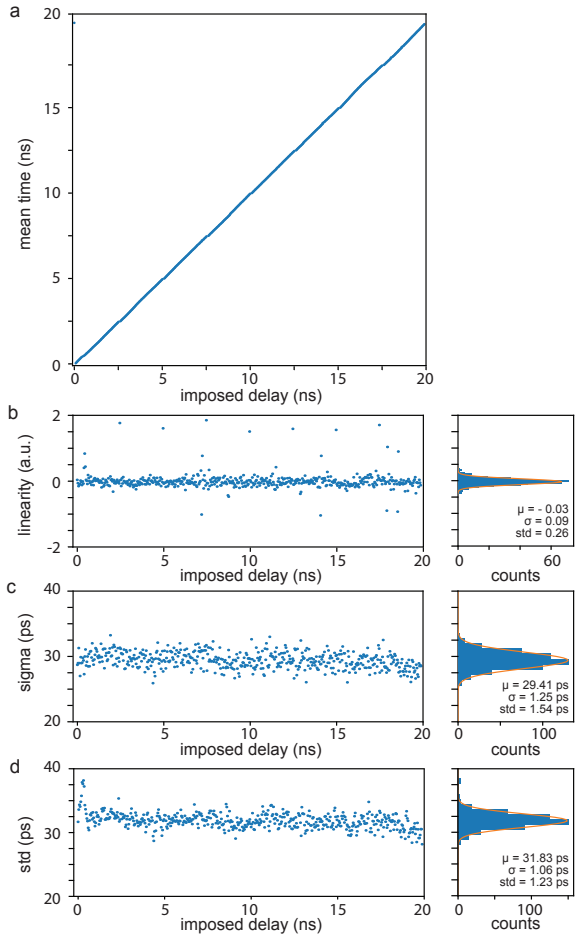


Fig. S1. Single Shot Precision Measurement. Detailed representation of the single-shot precision experiment for the photon channel #10. The experiment uses the BrightEyes-TTM to repeatedly measure the start-stop interval (i.e., the delay) between a fixed 50 MHz signal, used as SYNC signal, and a synchronised second signal, used as photon signal. The experiment is repeated for all possible delay values (imposed delay) within the repetition rate of the SYNC signal. For each imposed delay values, the TTM collects several millions of sync-photon pairs, and builds the start-stop time histograms (not shown). Each single histogram is fitted with a normal (Gaussian) distribution $A \exp\{-(t - \mu)/\sigma^2/2\}$ to extract the mean μ and the standard deviation σ values. (a) The mean value μ as a function of the imposed delay. (b) The difference between the imposed delay and the mean value obtained as function of the imposed delay. (c) The standard deviation σ value as function of the imposed delay. (d) Calculated standard deviation of the start-stop time histogram as a function of the imposed delay. The similar values between the Gaussian standard deviation σ and the calculated standard deviation demonstrates the normal distribution of the start-stop time histogram. One the right-side of each graph the relative statistics is reported.

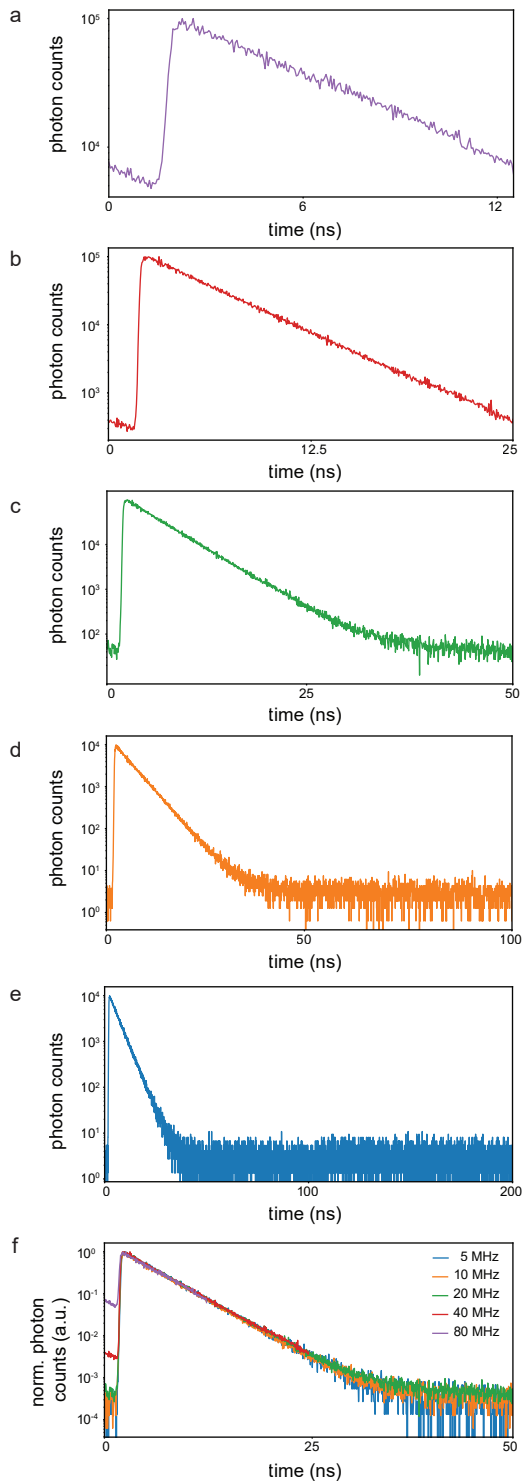


Fig. S2. Validation of TTM for different temporal ranges (a-e) and comparison of the obtained results (f). Fluorescence decay histogram (photon counts as a function of time) of a fluorescein-water solution for **a** 80 MHz, **b** 40 MHz, **c** 20 MHz, **d** 10 MHz and **e** 5 MHz laser repetition rates. **f** cumulative view (normalized photon counts versus time) of the reconstructed fluorescein decay histograms for all the probed temporal ranges. 40 MHz and 80 MHz curves show an higher offset when compared with 5, 10, and 20 MHz plots, due to a not complete relaxation of the fluorescein molecules from the excited state that occurs with shorter laser excitation periods.

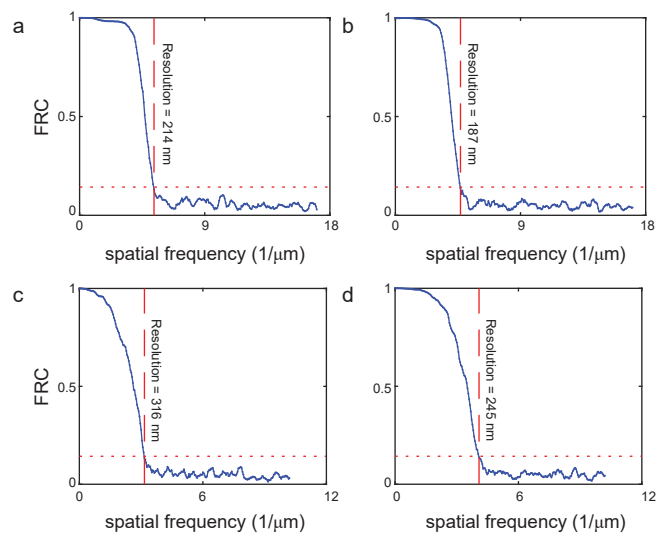
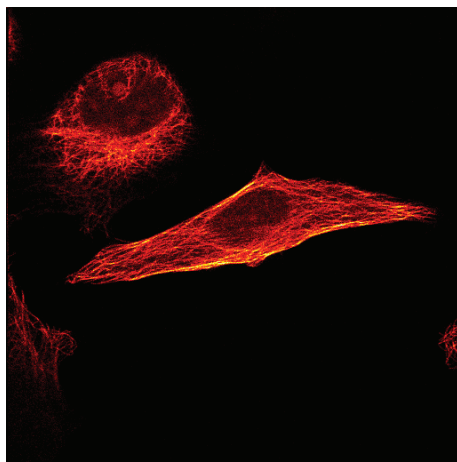


Fig. S3. Fourier ring correlation (FRC) analysis for ISM and confocal images of YG carboxylate fluoSpheres (a-b) and fixed-cells labelled for vimentin visualisation (c-d). The analysis compares side-by-side the FRC analysis for the confocal closed pinhole (0.2 AU) images (left) and the APR-ISM images (right). Each curve represents the decay of the correlation as a function of the spatial frequency. We used the 1/7 criteria (short dotted red lines) to estimate the effective cut-off frequencies of the images. The inversion of these values, which are reported in each graph, represents the effective resolution of the images.

a

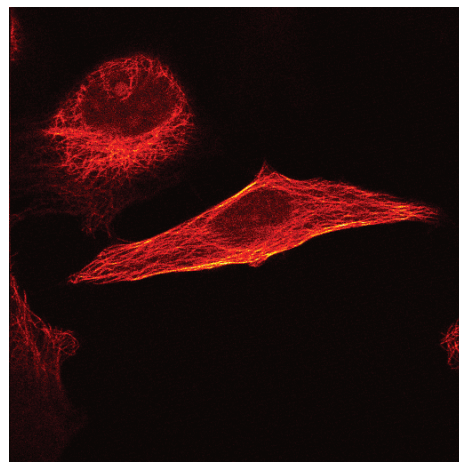
0 intensity (photons/200 µs) 109



BrightEyes-TTM

b

0 intensity (photons/200 µs) 107



NI card

Fig. S4. Imaging with the BrightEyes TTM and the real-time NI-DAQ systems. Side-by-side comparison of confocal (0.2 AU) images obtained with our TTM (a) and the NI-DAQ systems (b). The images represent a α -tubulin immunolabelled HeLa cell. The images were collected simultaneously: The BrightEyes-TTM receives the signal from the central element of the SPAD array detector, duplicates it, sends one copy back to the NI-DAQ system, while using the original signals to create the time-tagged data-set. The NI-DAQ system generates in real-time the confocal images, whilst the TTM image is generated off-line.

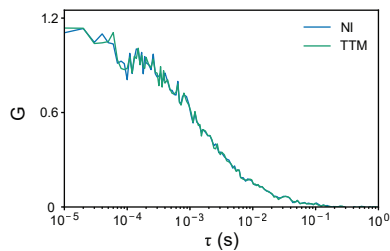


Fig. S5. Single-spot fluorescence correlation spectroscopy with the BrightEyes-TTM and NI-DAQ system. Comparison of the two autocorrelation curves obtained recording the simultaneously the signal with the two different platforms. The autocorrelation curves represent the signal collected from the central element of the SPAD array detector, and describe the freely diffusing fluorescent beads. Average over 13 traces of 10 s each.

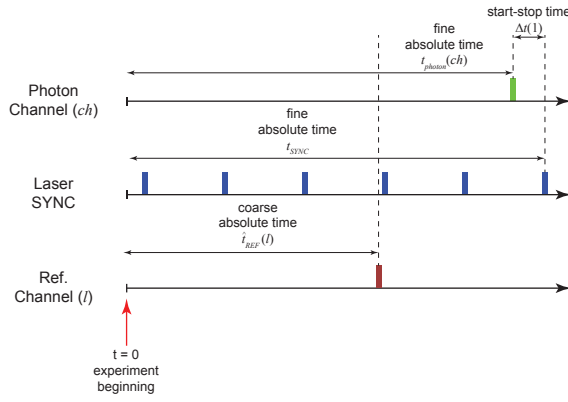


Fig. S6. Time-Tagging Principle. The time-tagging mode allows recording individual events and labelling each one of them with a temporal signature. Typically, this temporal signature denotes the time delay of the events in respect to the beginning of the experiment (absolute time). Our TTM is able to tag three different classes of events: The photon events, i.e., a photon is registered by the detector which delivers a digital signal to the module; The sync laser events, i.e., the synchronisation signal delivered by a pulsed laser; the reference events, i.e., a signal generated by another component of the experimental setup (e.g., an actuator, a laser modulator). Each class of events reports the temporal signature with a different precision: in our TTM the absolute times for the photon events (t_{photon}) and the laser synchronisation events (t_{SYNC}) have just few tens of picosecond precision, while the absolute time for the reference events (t_{REF}) has few nanosecond precision. Starting from these temporal signatures, it is possible to derive other several additional temporal information. For example, for each photon event, it is possible to derive the so-called start-stop time (Δt), which describes the delay of the photon event in respect to the successive sync laser event. Table 3 describes the main temporal signatures used in this work. Importantly, together with the temporal signatures, the TTM records also the number of the channels (ch) or inputs (l) associated to the photon or reference event. In our work, the channel for the photon event describes the spatial signature of the detected photon, as it contains the element of the SPAD array detector which collected the photon.

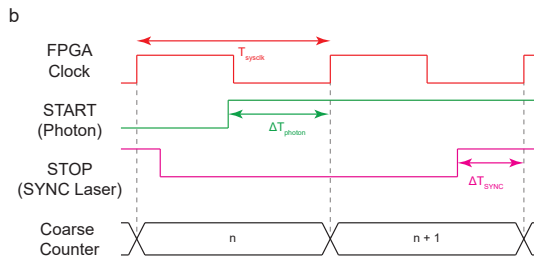
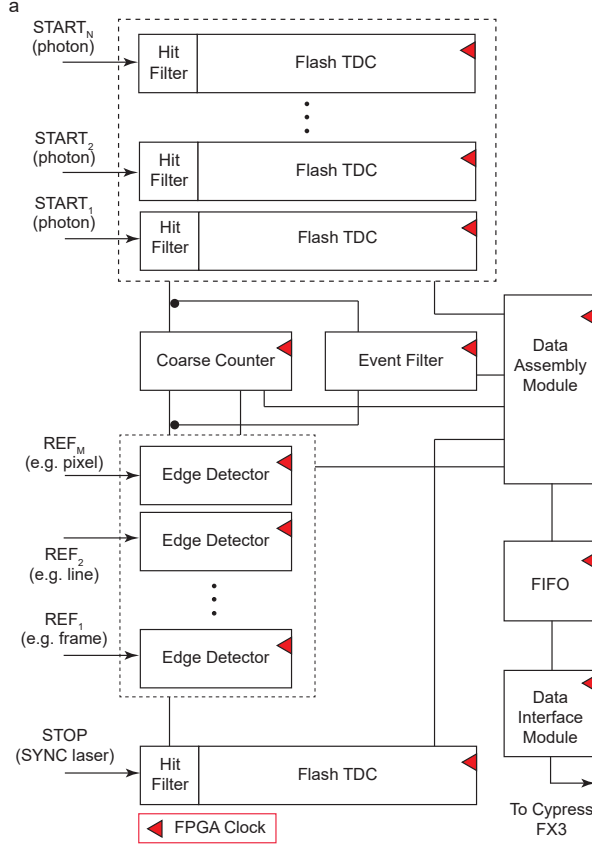


Fig. S7. Interpolating TTM-TDC FPGA architecture (a) and general fundamental concept of the sliding scale approach (b). **a** General and simplified architecture of the FPGA-based BrightEyes-TTM. Tapped delay line-based flash TDC modules and relative hit-filters for sampling the START_N ($N = 21$) signals, with picosecond precision, with respect to the FPGA clock (FPGA clock in red) (top portion of the figure). Free running coarse counter for implementing the sliding scale TDC technique and for sampling the REF_M ($M = 3$) synchronisation signals with a nanosecond precision (~4.2 ns). Event-filter circuit to reduce the data throughput by transmitting information only when photons are detected (middle-top portion). Edge detector components for sampling external reference signals with nanosecond precision (i.e. pixel, line, frame clock of an imaging SP-LSM system) using a counter-based coarser TDC approach (middle-bottom portion). Single tapped delay line (hit-filter & flash TDC module) for acquiring (with picoseconds precision) the STOP signal shared by all the START_N inputs (bottom). Data assembly module for collecting a multiplicity of input digital signals and values (i.e. $\Delta T_{\text{START}}(ch)$ and $n_{\text{photons}}(ch)$ as well as valid arrival flags for the photons, ΔT_{STOP} and n_{SYNC} as well as its valid digital flag for the laser sync, and the valid arrival flags for the REF_M signals) and arranging the digital data tags into a suitable form in order to be stored into a FIFO memory. FIFO memory to buffer incoming data waiting to be sent over a host-processing unit via the data interface module through the Cypress FX3 chip (right). **b** TTM interpolating architecture working principle. FPGA clock used (i) to drive all the TTM architecture components and (ii) as a fundamental reference signal for all the time measurements (top). Representation of how the TTM circuit architecture tags the START-photon (green) and STOP-sync (pink) signals with respect to the FPGA sampling clock (middle) while saving and computing both the ΔT_{START} and ΔT_{SYNC} (i.e. integer values representing the number of tapped-delays - in the delay line - that the signals have travelled through before the arrival of the FPGA clock rising-edge). Coarse free-running counter increasing its value at each FPGA clock rising-edge event for reconstructing, in a post-processing phase, Δt photon start-stop time.

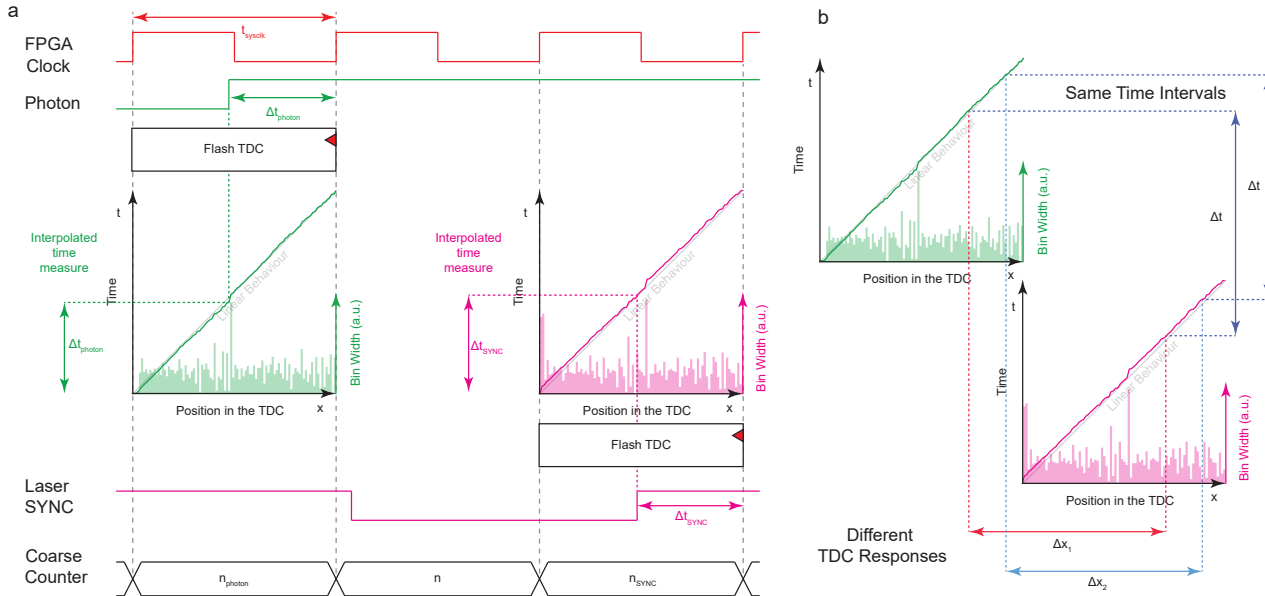


Fig. S8. Schematic of TTM sliding scale technique working principle (a) and mapping of $\Delta t(ch)$ start-stop time across START_N and $\text{STOP}_{\text{SYNC}}$ tapped-delay-lines (b). **a** The START_N (photon) arrival time ($\Delta t_{\text{START}}(ch)$) is computed with respect to the rising-edge of the FPGA clock (top) thanks to a dedicated flash-TDC module. Here, the time response and the tapped-delay-line bin widths are shown as a function of the bin number (left-middle). As soon as a START_N is detected also the value $n_{\text{photon}}(ch)$ of the coarse counter gets registered (bottom). The $\text{STOP}_{\text{SYNC}}$ arrival time (Δt_{SYNC}) is also recorded, on a dedicated flash-TDC module (time response and bin-widths are show in the right-bottom portion), with respect to the FPGA clock together with the corresponding value of the coarse counter n_{SYNC} (bottom). $\Delta t_{\text{START}}(ch)$, $n_{\text{photon}}(ch)$, Δt_{SYNC} and n_{SYNC} are used to compute $\Delta t(ch)$ (i.e. the start-stop time) according to Suppl. Eq. S1. **b** Smoothing out flash-TDC non-linearity: because of the START_N and $\text{STOP}_{\text{SYNC}}$ signals are asynchronous with respect to the FPGA clock, the same start-stop time interval Δt , (i.e. the delay between a photon and a laser sync event) is measured at different positions in the flash TDC modules.

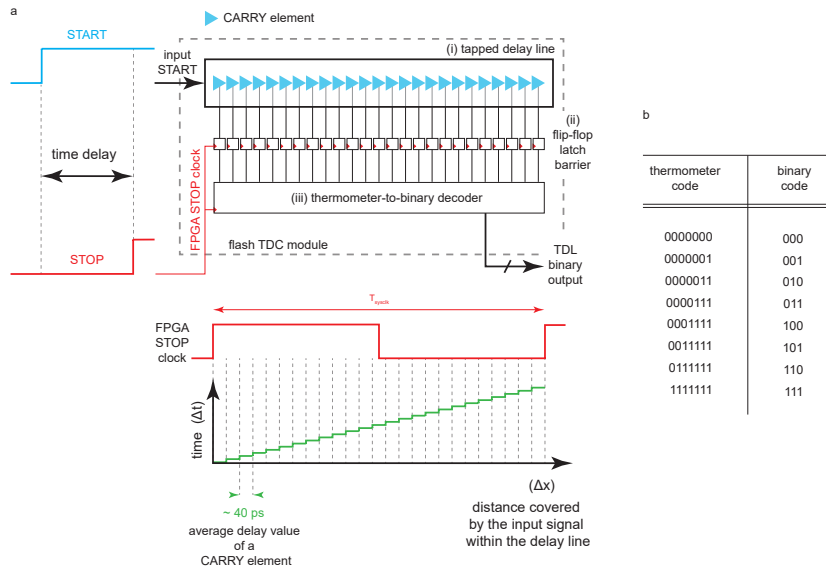


Fig. S9. Architecture of the flash time-to-digital (TDC) converter (a) and functioning of the thermometer-to-binary encoder (b). **a** Schematic representation of a delay line TDC constituted by (i) a tapped-delay line composed by inbuilt FPGA CARRY-delay elements, (ii) a flip-flop latch barrier to sample and stabilise the tapped-delay-line readings (i.e. $\Delta T_{\text{START}}(ch)$ or ΔT_{STOP}) and (iii) thermometer-to-binary encoder to translate the tapped-delay-line readings into a binary form (top); working principle of an TDL-TDC: the input signal propagates along the TDL until reading event occurs. By knowing the reciprocal relationship between the CARRY delay value and the distance the input signal covered before the STOP event occurred, it is possible to convert the digital measurement of the travelled distance into a time measurement (bottom). **b** Example of thermometer-to-binary working principle: tapped-delay-line readings are converted into binary number for a more compact and efficient data representation.

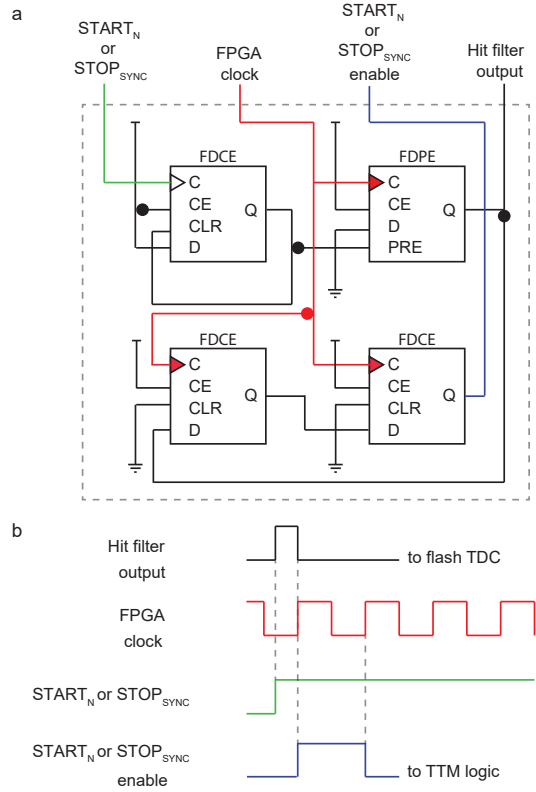


Fig. S10. Schematic circuit of the hit filter component (a) and related input-output digital signals (b). **a** Hit-filter FPGA digital circuit. The intimate digital-electronic layout of the hit-filter is made only by four flip-flops. The hit-filter component is engineered and deployed to shape the incoming photons and sync signal lengths based on the sampling FPGA clock period and, at the same time, to generate a toggle signal event (the photon or sync enable signal) for each detected START_N (photons) and $\text{STOP}_{\text{SYNC}}$ (sync) events. The hit-filter logic is also necessary to avoid the clogging of the flash TDC module and to allow for the TDC module to be ready to sample incoming signals, thus reducing the dead-time of the architecture. Thanks to the hit-filter, the architecture is independent from the signal pulse duration (hold-off). While the hit filter output signal is solely used to activate the flash TDC module, the photon enable signal is distributed to the entire TTM logic to sample and record the arrival of a photon (or sync pulse) on a specific channel. **b** Input and outputs signals of the hit-filter logic. Primary digital hit-filter output (top), sampling FPGA clock (second row), rinsing edge of photon or sync event (third row), photon or sync enable signal that has the duration of an FPGA clock period (bottom).

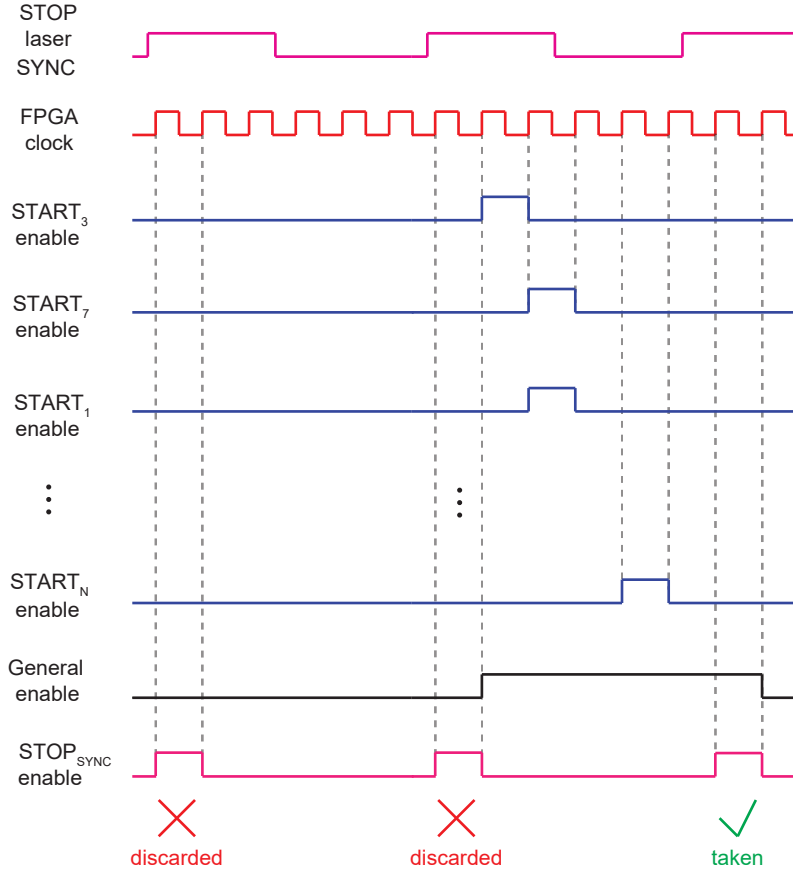


Fig. S11. Logic circuit of the event filter component. All valid-enable photon signals (from START_1 enable to START_N enable), produced by the hit-filter modules whenever a START-photon (or $\text{STOP}_{\text{SYNC}}$) event is detected, are used to efficiently record the multi-channel data tags ($\Delta T_{\text{START}}(ch)$ and ΔT_{STOP}). The event filter was designed and implemented to optimally handle time-tag data for high repetition rates of the laser sources (up to 80 MHz - Suppl. Fig. S2) used in SP-LSM applications. It is not efficient to sample and tag all the incoming laser pulses (laser SYNC events) and stream the related information together with the data tags ($\Delta T_{\text{START}}(ch)$, ΔT_{STOP} , $n_{\text{photon}}(ch)$, n_{SYNC}) of sampled photons to a processing unit. For this reason, the event filter circuit works backwards: when a photon is detected in the i channel, the corresponding START_i enable activates a general enable signal. The general enable signal remains active until the detection of a successive laser pulse sync signal ($\text{STOP}_{\text{SYNC}}$ enable). If the general enable signal is high at the moment of a $\text{STOP}_{\text{SYNC}}$ pulse, at least one photon has been detected and only in this case the FPGA circuit tags and registers the START-STOP times of all photons in all channels. By discarding $\text{STOP}_{\text{SYNC}}$ events that do not have a corresponding START_i enable event the data rate can be significantly reduced.

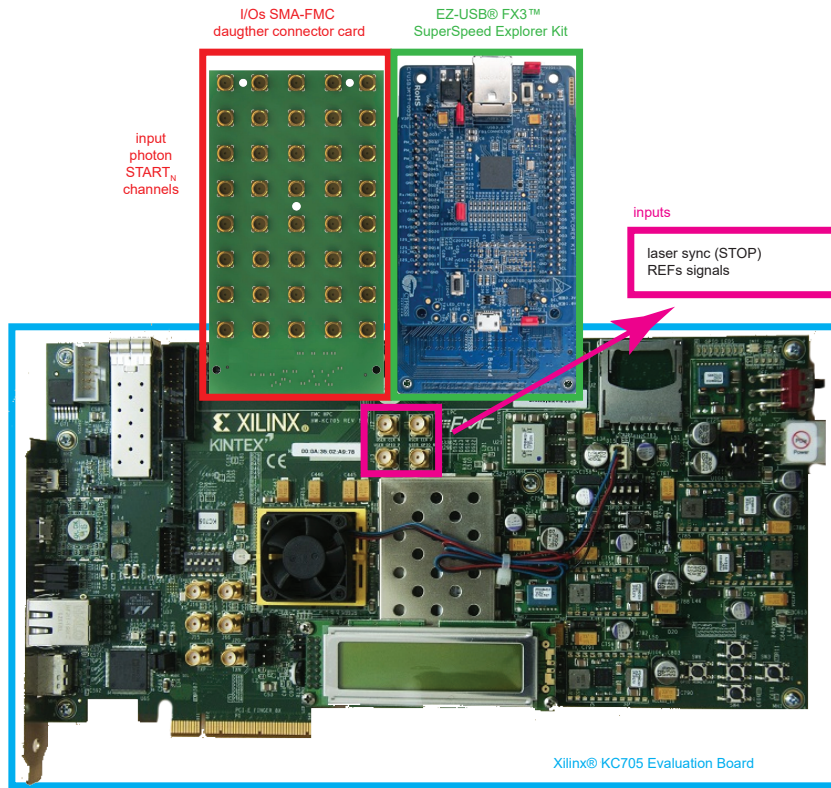


Fig. S12. BrightEyes-TTM final assembly. The Xilinx® KC705 Evaluation board, the Cypress® FX3™ SuperSpeed Explorer Kit and the connector card can be easily stacked together, using FMC connectors which interlock the three components. REF_M and laser SYNC signals are directly connected to the main board using dedicated SMA connectors.

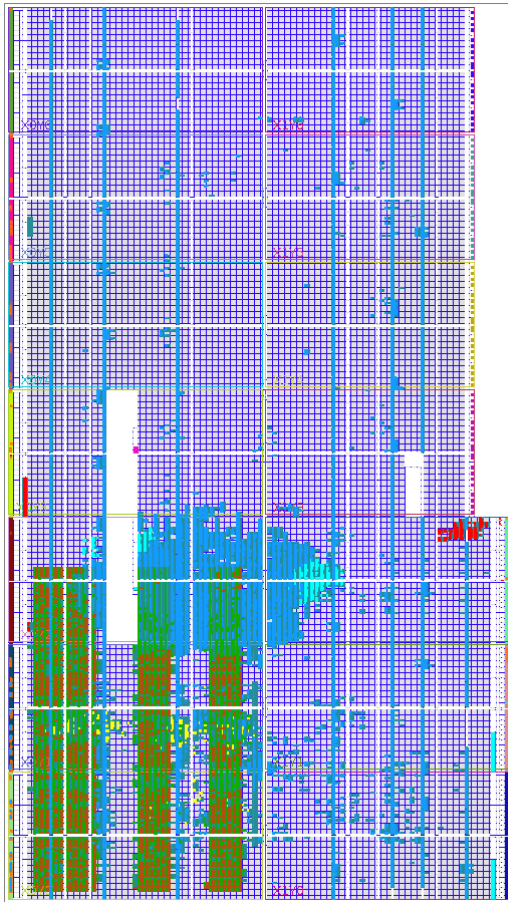


Fig. S13. FPGA resource utilisation. 20% of slice look-up-tables (LUT) for TDLs (dark red) and T2B in green; FIFO (98% of inbuilt BRAM) and 5% of LUT for FX3 module in light-blue; Integrated logic analyser (ILA) debugger in yellow; SYLAP (only for test purpose) in red - 2% LUT.

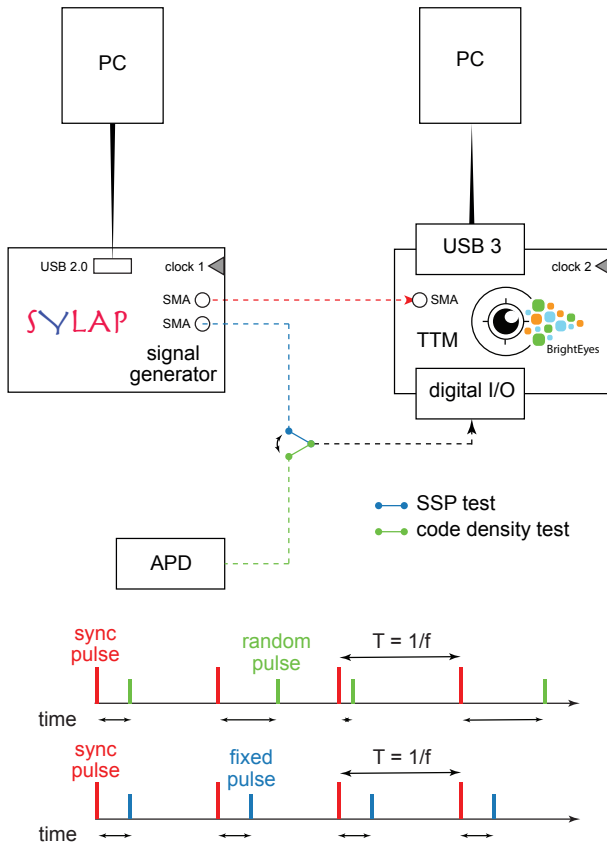


Fig. S14. Test Bench System. The setup used for the TTM tests and characterisations. The TTM STOP is connected to clock generated by SYLAP. The TTM start input can be connected to an APD for generating asynchronized pulses (green); or can be connected to SYLAP to generate pulses with a fixed delay respect to the clock (blue).

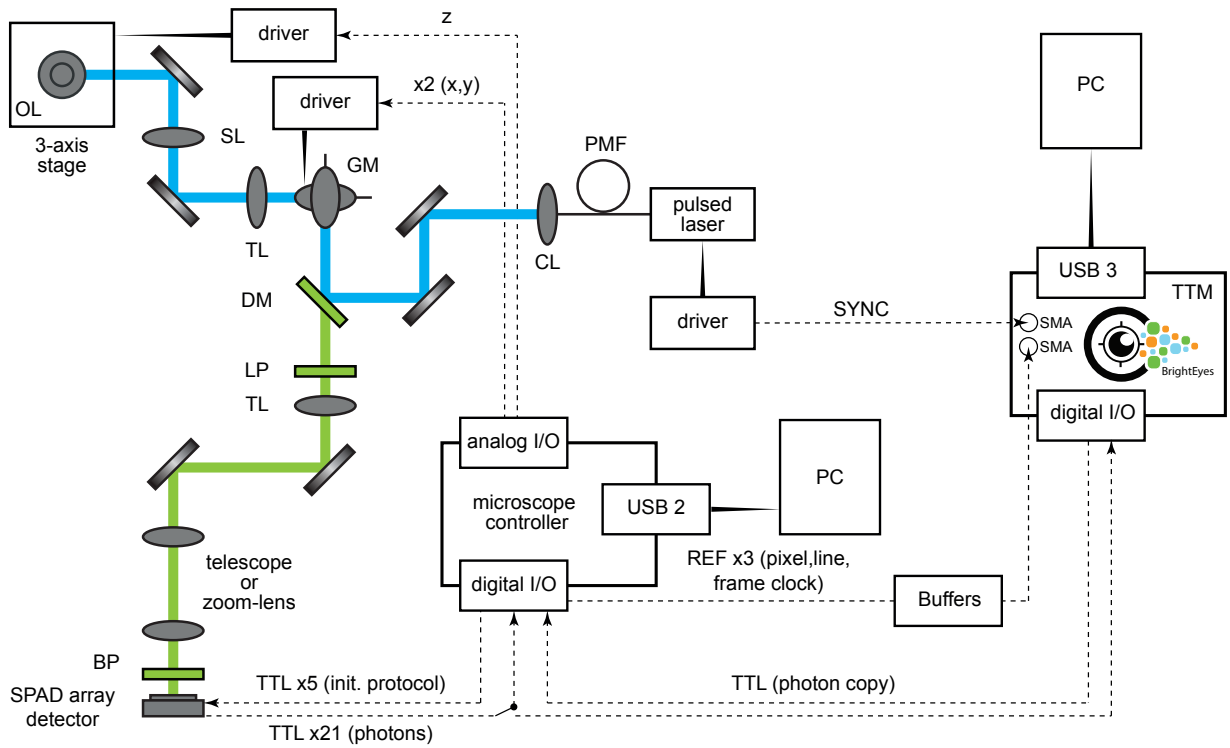


Fig. S15. Single-photon laser scanning microscope. Schematic representation of the optical architecture, the data-acquisition and control system. Digital and analogue single-cable connections are represented by dashed lines. DM: dichroic mirror, GM: galvanometric scan mirrors, SL: scan lens, TL: tube lens, OL: objective lens, LP: long pass filter, BP: band pass filter, CL: collimating lens, PMF: polarising maintaining fiber. The pixel, line, and frame reference signals and the laser sync signal are directly plugged to the FPGA-development board using the SMA user I/Os, whilst the photon signals are plugged to the board by using the I/Os daughter card. The board duplicates the photon signal from the central element of the SPAD array detector and send it back to the microscope controller via a TTL digital signal.

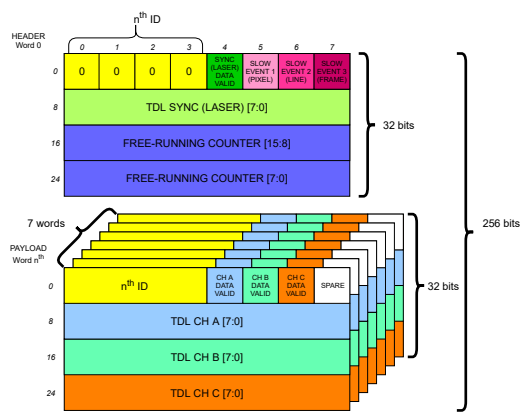


Fig. S16. Data Structure. The data structure has an header 32-bit word and, in case of 21 channels, seven payload 32-bits words each one identified with an associated ID number. The channel CH A, B, C are different in each payload words and they are sequentially corresponding to channels 0 ... 20.

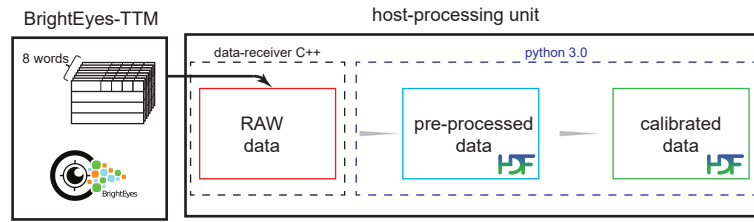


Fig. S17. Data processing pipeline. A low level data-format arranged in 8 words is streamed by the BrightEyes-TTM and saved into a raw-data form using a C++ based software program. Raw data gets pre-processed and refined in a python-based analysis environment for data calibration and further data reconstruction.

RAW DATA

FREE-RUNNING COUNTER	SLOW EVENT 1 (PIXEL)	SLOW EVENT 2 (LINE)	SLOW EVENT 3 (FRAME)	SYNC DATA VALID	TDL SYNC (LASER)	CH1 DATA VALID	TDL CH 1	CH2 DATA VALID	TDL CH 21
19325				1	41	1	17		
19326								1	32
19327						1	54		
19328							1	27	
19329				1	19				
19330	1			1	29	1	11	1	9
19331				1				1	54
19332				1	37	1	7		
19333	1			1	13			1	8
...

PRE-PROCESSED DATA SAVED IN SEPARATED TABLE

MAIN						CH1			CH...			CH21		
idx	x	y	fr	n	ΔT_{STOP}	idx	Δn	ΔT_{START}	idx	Δn	ΔT_{START}	idx	Δn	ΔT_{START}
1	34	54	3	19325	41	1	0	17	2	1	27	2	3	32
2	34	54	3	19329	19	2	2	54	3	0	11	3	0	9
3	35	54	3	19330	29	3	0	11	4	0	7	4	1	54
4	0	0	4	19332	37	4	0	7	5	1	8	5	0	8
5	1	0	4	19333	13									
...					

CALIBRATED DATA SAVED IN SEPARATED TABLE

MAIN					CH1			CH...			CH21			
idx	x	y	fr	$t_{sync} [ps]$	idx	$\Delta t[ps]$	idx	$\Delta t[ps]$	idx	$\Delta t[ps]$	idx	$\Delta t[ps]$	idx	$\Delta t[ps]$
1	34	54	3	80520833.3	1	1152.0	2	3782.7	2	11876.0	3	960.0	4	3350.7
2	34	54	3	80537500.0	2	6653.3	3	864.0	3	...	4	240.00	5	...
3	35	54	3	80541666.7	3	1440.0	4	...	4	...	5	...	5	...
4	0	0	4	80550000.0										
5	1	0	4	80554166.7										
...										

Fig. S18. Data pre-processing. The table in the top represents the raw data as received. In the top table, the grey cells are the data-valid flags. Each SYNC data-valid flags (in dark grey) is associated to a new unique index (number yellow highlighted). The tables in the middle (main and channels tables) represent the data after the pre-processing. Notably, the channels tables have not all indexes, as they contains only valid events. The tables in the bottom represents the calibrated data.

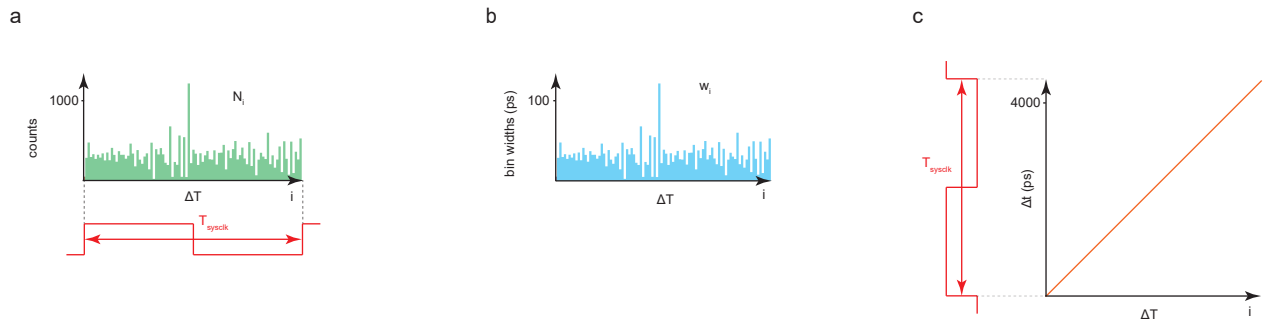


Fig. S19. Main steps of the bin-by-bin calibration procedure. **a** Tapped-delay-line histogram of received counts as a function of the arrival tap (delay) number. The range of the maximum arrival tap number depends on the reference FPGA clock period T_{sysclk} : the dimension of the tapped-delay-line are equal to the total delay value of T_{sysclk} . **b** Estimation of the individual value w_i of each delay element. **c** Time as a function of ΔT : each w_i is used to compute the $\Delta t_{\text{START}}(ch)$ or Δt_{SYNC}

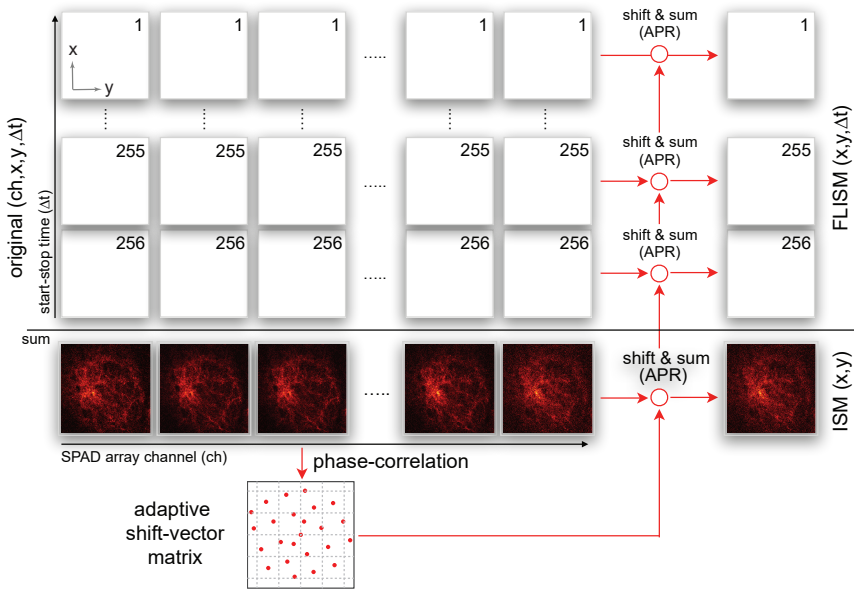


Fig. S20. Adaptive pixel-reassignment method for 4D lifetime data-set. In case of imaging, the BrightEyes-TTM provides a 4D ($ch, x, y, \Delta t$) pre-processed data-set, which can be used to reconstruct the high-resolution FLISM image. The reconstruction consists in the following steps. (i) The algorithm integrates the data-set along the start-stop Δt dimension, and generates a 3D (ch, x, y) data-set; (ii) a phase-correlation registration algorithm uses the conventional intensity data-set to calculated the shift-vector fingerprint ($s_x(ch), s_y(ch)$); (iii) for each Δt the images (x, y) associated to each channel ch are shifted according to the shift-vector fingerprint and summed (i.e, along the ch dimension). The result is a 3D ($x, y, \Delta t$) which can be used to calculate the lifetime map or the phasor-plot histogram.

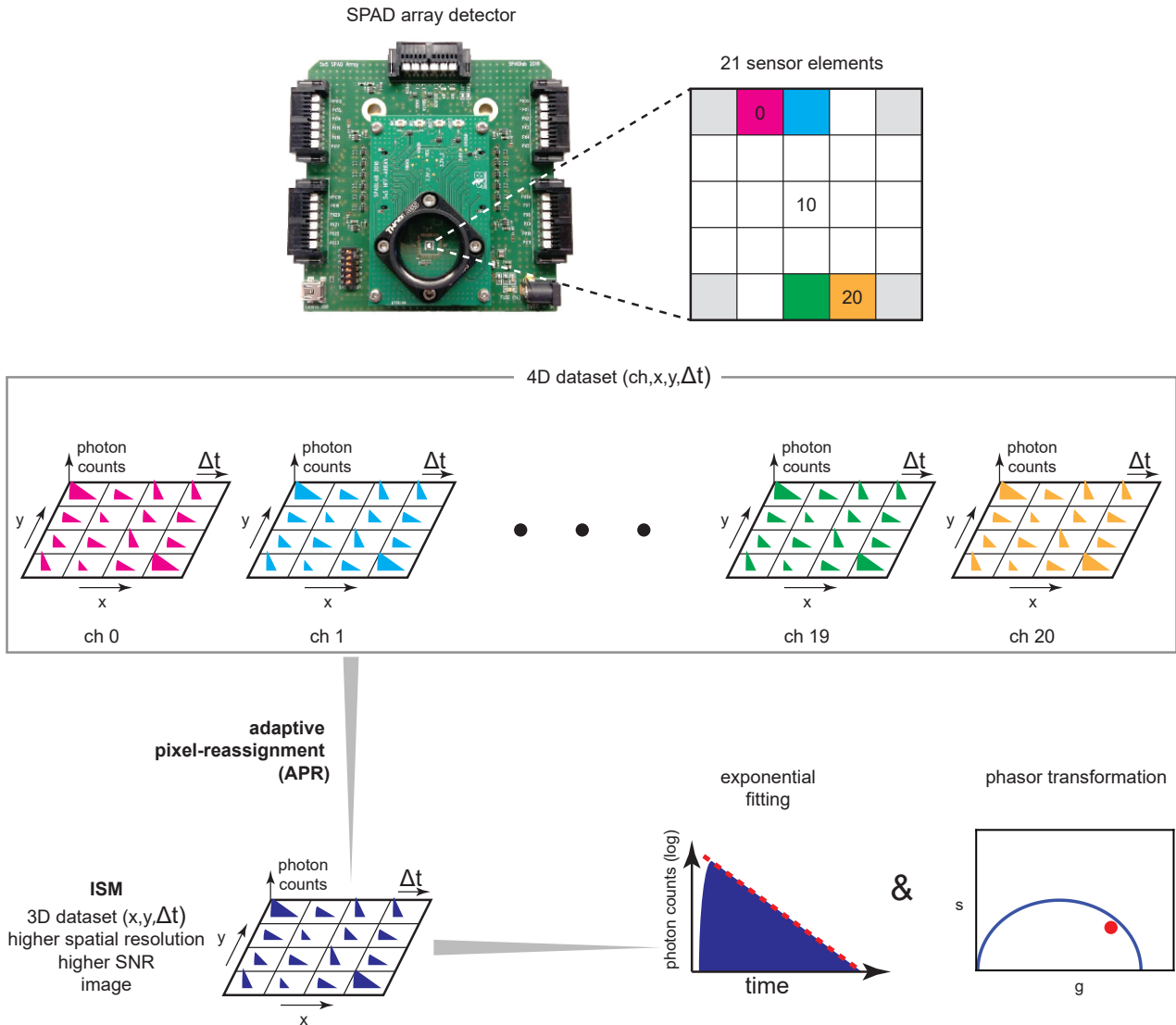


Fig. S21. 4D imaging dataset processing. By sampling the photon flux coming from the 21 elements of the SPAD array in combination with the REFs signals, the BrightEyes-TTM is able to reconstruct, in a post-processing phase, a 4D photon dataset ($ch, x, y, \Delta t$). The pixel reassignment methodology is used to transform the 4D data into a 3D ($x, y, \Delta t$) ISM intensity image which is fitted with an exponential model and phasor-transformed in order to extract the lifetime information.

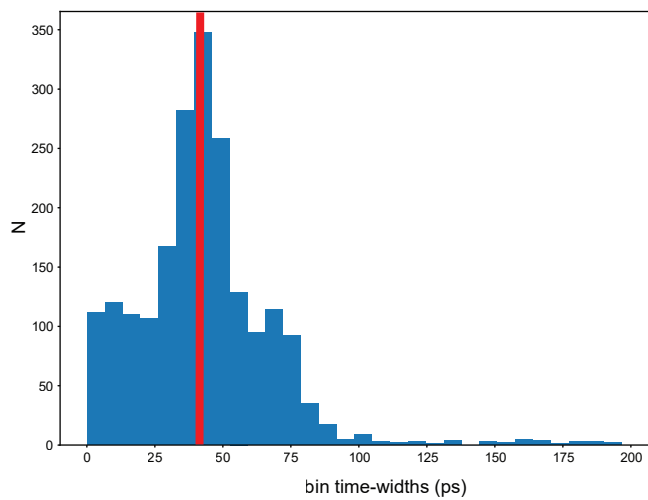


Fig. S22. Histogram of the time-bin widths (w_i) of all the deployed TDLs in the TTM architecture. Cumulative histogram, number (N) as a function of time-bin widths, of all the calculated w_i for all the TTM delay lines. The histogram mean value (red line) is $w_{\text{avg}} = 43 \pm 25$ ps.

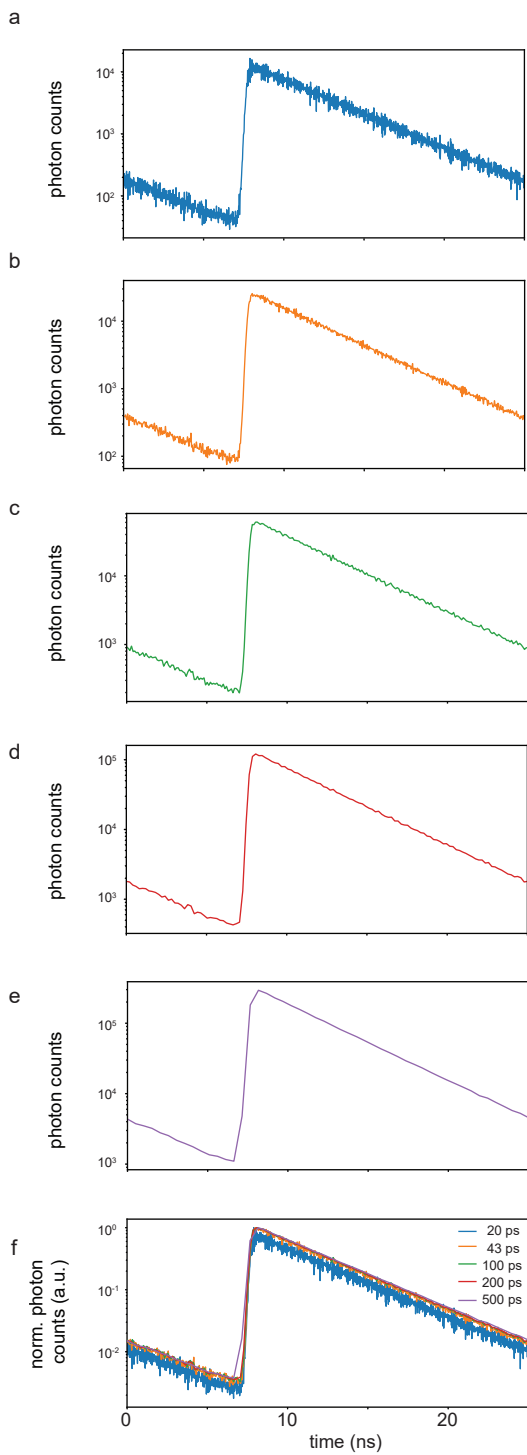


Fig. S23. TCSCP histograms of a fluorescein solution reconstructed using different time bin widths (a-e) and superposition of the obtained results (f). Fluorescence decay histogram (photon counts as a function of time) of a fluorescein-water solution reconstructed with bin-width of **a** 20 ps, **b** 43 ps, **c** 100 ps, **d** 200 ps and **e** 500 ps. **f** cumulative view (normalised photon counts versus time) of the reconstructed fluorescein decay histograms for all the different tested time bin-widths. The smaller the time bin-width the higher the SNR. The 20 ps curve shows a noisier profile when compared to 43, 100, 200 and 500 ps curves, due to an undersampling of the actual bin-width for the reconstructed TCSPC histograms.

Table 1. Notations

$\Delta T_{\text{START}}(ch)$	integer value representing the number of tapped-delays (in the START tapped-delay line) that the START signal, i.e., the photon signal, already travel through before the arrival of the FPGA clock signal. When reported, ch denotes the photon channel.
$\Delta t_{\text{START}}(ch)$	calibrated temporal value representing the time elapsed from the START signal, i.e., the photon signal, and the next active edge of the free-running coarse counter (FPGA clock). When reported, ch denotes the photon channel.
ΔT_{STOP}	integer value representing the number of tapped-delays (in the STOP tapped-delay line) that the STOP signal, i.e., the laser SYNC signal, already travel through before the arrival of the FPGA clock signal.
Δt_{STOP}	calibrated temporal value representing the time elapsed from the STOP signal, i.e., the laser SYNC signal, and the next active edge of the free-running coarse counter (FPGA clock).
$\Delta t(ch)$	photon start-stop time, i.e., the photon arrival-time in reference to the excitation event. When reported, ch denotes the photon channel.
$\hat{t}_{\text{photon}}(ch)$	photon-arrival time with respect to the beginning of the experiment measured with nanosecond precision (by using only the free-running course counter). When reported, ch denotes the photon channel.
$\hat{t}_{\text{SYNC}}(ch)$	SYNC-arrival time with respect to the beginning of the experiment measured with nanosecond precision (by using only the free-running course counter).
$\hat{t}_{\text{REF}}(l)$	REF-arrival time with respect to the beginning of the experiment measured with nanosecond precision (by using only the free-running course counter).
$\Delta \hat{t}_{\text{REF}_l}^{\text{photon}}(ch)$	photon-arrival time with respect to the l -th reference event measured with nanosecond precision (by using only the free-running course counter). When reported, ch denotes the photon channel.
$n_{\text{photon}}(ch)$	the number of FPGA clock cycle between the beginning of the experiment and the photon signal. When reported, ch denotes the photon channel.
n_{SYNC}	the number of FPGA clock cycle between the beginning of the experiment and the laser SYNC signal.
n_{REF_l}	the number of FPGA clock cycle between the beginning of the experiment and the l -th reference signal.
$\Delta n(ch)$	the number of elapsed FPGA clock cycle from the START photon event and the relative STOP laser SYNC event. When reported, ch denotes the photon channel.
T_{sysclk}	the period of the FPGA system clock.
f_{sysclk}	frequency of the FPGA system clock.
$t_{\text{photon}}(ch)$	absolute time from the beginning of the experiment for the photon signal with, in principle, picosecond precision.
t_{SYNC}	absolute time from the beginning of the experiment for the SYNC signal with, in principle, picosecond precision.
(x, y, z)	spatial coordinate for the scanning system.
fr	frame.
τ_{fl}	fluorescence excited-state lifetime, i.e., average time that a fluorophore spend in the excited state. Assuming a single exponential decay it represent the inverse of the decay rate.
\mathcal{T}	the period of the pulsed excitation laser.
f	the frequency of the pulsed excitation laser.
τ_D	diffusion (or transient) time, in the context of FFS.
D	diffusion coefficient, in the context of FFS.
ω	detection volume lateral size, in the context of FFS .